The Astrophysical Journal, 975:217 (19pp), 2024 November 10 https://doi.org/10.3847/1538-4357/ad7b15

Determining the Magnetic Field in the Galactic Plane from New Arecibo Pulsar Faraday Rotation Measurements

Alice P. Curtin[1,2,3], Joel M. Weisberg[3], and Joanna M. Rankin[4]
[1] Department of Physics, McGill University, 3600 rue University, Montréal, QC H3A 2T8, Canada; alice.curtin@mail.mcgill.ca
[2] Trottier Space Institute, McGill University, 3550 rue University, Montréal, QC H3A 2A7, Canada
[3] Department of Physics and Astronomy, Carleton College, Northfield, MN 55057, USA
[4] Department of Physics, University of Vermont, Burlington, VT 05405, USA
Received 2024 July 16; revised 2024 September 13; accepted 2024 September 13; published 2024 November 5

Abstract

We develop a new method for studying the Galactic magnetic field along the spiral arms using pulsar Faraday rotation measures (RMs). Our new technique accounts for the dot-product nature of Faraday rotation and also splits the associated path integral into segments corresponding to particular zones along the line of sight. We apply this geometrically corrected, arm-by-arm technique to the low-latitude portion of a recently published set of Arecibo Faraday RMs for 313 pulsars, along with previously obtained RMs in the same regions. We find disparities $>1\sigma$ between the magnitude of the field above and below the plane in the Local Arm, Sagittarius Arm, Sagittarius-to-Scutum Interarm, Scutum Arm, and Perseus Arm. We find evidence for a single field reversal near the Local Arm–Sagittarius Arm boundary. Interestingly, our results suggest that this field reversal is dependent on latitude, occurring inside the Sagittarius Arm at negative Galactic latitudes and at the Local Arm–Sagittarius Arm boundary at positive Galactic latitudes. We discuss all of our results in the context of different models and other observational Galactic magnetic field analyses.

Unified Astronomy Thesaurus concepts: Radio pulsars (1353); Milky Way magnetic fields (1057); Interstellar medium (847); Radio astronomy (1338)

1. Introduction

Pulsars are excellent probes of the magnetic field in the plane of the Galaxy, due to the phenomena of Faraday rotation and dispersion. A radio source's Faraday rotation measure (RM), measured in radians per square meter (rad m^{-2}), can be determined via observations of the rotation of its linear plane of polarization as a function of frequency and is related to the vector magnetic field, sampled along the line of sight (LOS), as follows:

$$\mathrm{RM} = \frac{e^3}{2\pi m_e^2 c^4} \int_{\mathrm{source}}^{\oplus} n_e \boldsymbol{B} \cdot d\boldsymbol{s}, \tag{1}$$

where e and m_e are the electron charge and mass, respectively, c is the speed of light, n_e is the free electron density, $\boldsymbol{B}$ is the magnetic field, and ds is an element of path length along the source−observer LOS (D. R. Lorimer & M. Kramer 2012).

A pulsar's dispersion measure (DM), measured in parsecs per cubic centimeter (pc cm^{-3}), can be determined from observations of the pulse delay as a function of frequency and is related to the electron density along the LOS through (D. R. Lorimer & M. Kramer 2012)

$$\mathrm{DM} = \int_{\mathrm{source}}^{\oplus} n_e \, ds. \tag{2}$$

Specifically, Equations (1) and (2) indicate that a pulsar's Faraday-rotated, dispersed signals reveal the mean of the magnetic field magnitude $|B|$ multiplied by a cosine term originating from the dot-product nature of Equation (1):

$$\langle |B| \cos\theta_{B\cdot ds} \rangle = 1.232 \, \frac{\mathrm{RM}}{\mathrm{DM}} \, \mu\mathrm{G}, \tag{3}$$

when RM and DM are measured in their usual units, rad m^{-2} and pc cm^{-3}, respectively, and where $\theta_{B\cdot ds}$ is the angle between the source−Earth LOS and magnetic field vectors. The angle brackets represent an average along the path over which RM and DM are evaluated. One can determine the mean magnetic field magnitude alone from Equation (3) if the geometry of the field (and hence the value of the cosine term) is known.

Polarized extragalactic radio sources (EGSs) allow measurement of the total RM, but this only reveals the integral of the rather complicated quantity ($n_e\,|B|\,ds\cos\theta_{B\cdot ds}$) along the full path from the source to the observer. This impedes any effort to disentangle the magnetic field from the other variables, especially in a particular Galactic zone. Pulsed sources such as pulsars and fast radio bursts are the only class of object for which a DM can be measured, and hence the only objects to which Equation (3) can be directly applied.

Furthermore, because pulsars are embedded within the interstellar medium of our Galaxy at approximately known distances, we can use groups of them to assess the systematic Galactic magnetic field along specific intragalactic zones such as spiral arms or interarm regions, including regions lying beyond other systematic magnetic zones. In this work, we present a new "arm-by-arm" technique for determining the systematic magnetic field along long stretches of spiral arms by correcting for the assumed field geometry and for the effects of nearer magnetic regions.

In a companion paper, J. Rankin et al. (2023) have taken advantage of the sensitivity of the Arecibo telescope and its

wide-bandwidth Gregorian feed and spectrometers to measure RMs of virtually all known low-latitude pulsars in the telescope's accessible decl. range, in addition to some higher-latitude sources. We use these new low-latitude measurements and all other relevant pulsar RM determinations in and near these directions to study the systematic Galactic magnetic field in these portions of the Galactic plane. We believe that our work represents the first geometrically corrected measurement of the systematic magnetic field magnitude along large stretches of spiral arms and interarm regions.

The plan of this paper is as follows. In Section 2, we discuss the measurements used in our Galactic magnetic field analysis. In Section 3, we first present our new "arm-by-arm" technique for studying the Galactic magnetic field. Then, in Section 4, we apply our technique to study the systematic field in the plane in and near our observed Galactic longitude ranges. In Section 5, we discuss our results within the larger context of Galactic field models. A summary is presented in Section 6.

2. Pulsar Rotation Measures, Distances, and Galactic Structure

2.1. Rotation Measures

J. Rankin et al. (2023) have determined the RMs of 313 pulsars within the field of view of Arecibo Observatory in the longitude ranges ∼30°–80° and ∼175°–210°. Their observations were carried out at frequencies near 0.3 and 1.5 GHz, beginning in early 2003 and concluding in late 2020. RMs and uncertainties for this set of pulsars can be found in Table 1 of J. Rankin et al. (2023). Figure 1 displays the Galactic locations of the pulsars from that work that we include in our analysis.

For the current analyses, the low-latitude ($|b| \leqslant 9°$) portions of these new RMs are supplemented by previously measured ones in the Galactic plane in nearby directions, taken from version 1.64 of the ATNF Pulsar Catalog (R. N. Manchester et al. 2005) plus a set of more recent observations (S. Johnston et al. 2021).[5] In the case of multiple RM values for a particular pulsar, we adopted that with the smallest uncertainty. While all pulsars studied will have $|b| \leqslant 9°$, the term "low latitude" will henceforth be omitted in most cases.

In addition to pulsars, we could also use the RMs from polarized EGSs to study the Galactic magnetic field. However, as our method (detailed in Section 3) explicitly depends on separating the LOS from a source into known segments, we do not rely on RMs from EGSs, except when commenting on others' work.

2.2. Additional Information

2.2.1. Distances

For almost all of the pulsars' LOSs, we adopted the "best" pulsar distance from version 1.64 of the ATNF Pulsar Catalog.[6] This distance is defined as the distance derived from the measured DM and the J. M. Yao et al. (2017, hereafter YMW17) electron density model, unless a more accurate distance is available from other techniques such as very-long-baseline interferometry (VLBI) parallax measurement, kinematic distance via H I 21 cm absorption, or association with another object of known distance.[7]

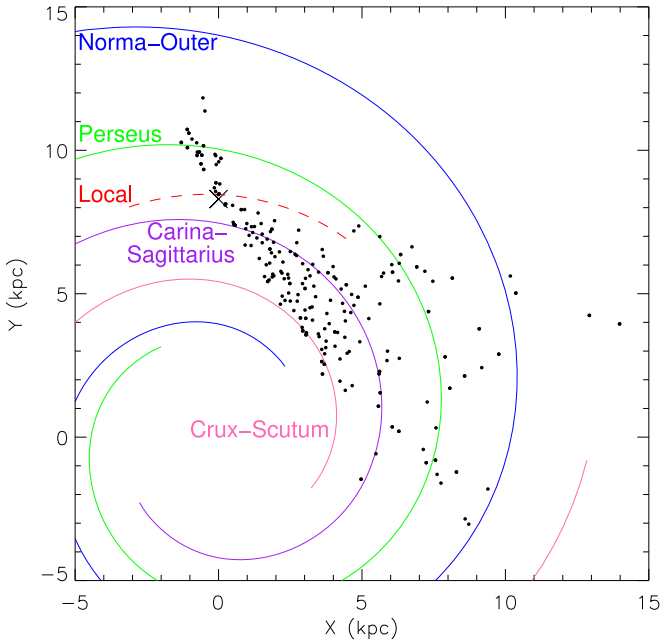

Figure 1. Locations of all low-latitude ($|b| \leqslant 9°$) pulsars measured and tabulated in J. Rankin et al. (2023). The solar system is marked by the black cross at $(x, y) = (0.0, 8.3)$ kpc. The plotted locations of the spiral arm centers are from YMW17 (J. M. Yao et al. 2017).

2.2.2. Galactic Structure

One of the major goals of this work is to study the nature of the systematic magnetic field associated with various Galactic structures, especially spiral arms and interarm regions. Hence, it is crucial to use the best available knowledge of these structures. With the exception of the Local Arm (see Section 4.1), we use the spiral arm centers as defined by L. G. Hou & J. L. Han (2014) and slightly modified by YMW17, with the solar system located 8.3 kpc from the Galactic center. The general logarithmic expression for the arm centers can be found in Equations (10a) and (10b), with the adopted values of constants therein, and Table 1 of the latter reference. The arm centers can also all be seen in Figure 1.

3. Arm-by-arm Galactic Magnetic Field Analysis

In this section, we develop a new technique for attributing portions of the path-integrated quantities RM and DM to specific arms and interarm regions along each pulsar's LOS. Once we determine the RM and DM attributable to each such zone, we are able to also measure the *B*-field associated with it.

[5] Some of the RMs reported in the ATNF Catalog include an unsubtracted ionospheric component, which indicates that some of the ATNF Catalog's RMs have larger uncertainties than quoted.

[6] This is denoted as "DIST" in that catalog.

[7] The single exception to these rules was PSR J2021+3651, where we replaced the ATNF Catalog's "DIST" value of 1.80 kpc with the YMW17 DM distance estimate of 10.51 kpc. This pulsar has a very high DM for its putative "DIST," which was derived from X-ray measurements of the hydrogen column density along the LOS (A. Kirichenko et al. 2015). Nevertheless, P. Kutukcu et al. (2022) also suggest a relatively high distance similar to ours, based on analogous considerations. While a localized electron density enhancement could explain the disproportionately high DM, there is no evidence of an H II region (S. K. Ocker et al. 2024) along the LOS. Similarly, we find no unusual H I column density (HI4PI Collaboration et al. 2016) along the LOS. We believe that it is more likely that the X-ray distance determination procedure, which is less well established than the DM distance technique, has rendered an unrealistically small distance. We note this one exception in Table 1 of J. Rankin et al. (2023).

Table 1
Fitted Mean Magnetic Fields in Selected Regions of the Galactic Plane ($|b| \leqslant 9°$)

Region	Section	Logarithmic Spiral Parameters for Equation (4)						Mean Magnetic Field[a]	
		$R_{0,\mathrm{inner}}$ (kpc)	$\phi_{0,\mathrm{inner}}$ (deg)	ψ_{inner} (deg)	$R_{0,\mathrm{outer}}$ (kpc)	$\phi_{0,\mathrm{outer}}$ (deg)	ψ_{outer} (deg)	For $-9° \leqslant b < 0°$ (μG)	For $0° \leqslant b \leqslant 9°$ (μG)
Local Arm	Section 4.1	3.880	218.3	10.38	3.407	119.9	9.84	-2.48 ± 0.42	-1.29 ± 0.62
Sagittarius Arm	Section 4.3	3.190	218.3	10.38	3.880	218.3	10.38	0.32 ± 0.32	1.88 ± 0.24
Sag.-to-Scut. Interarm	Section 4.4	2.760	218.3	10.38	3.190	218.3	10.38	1.00 ± 0.29	-0.25 ± 0.36
Scutum Arm	Section 4.5	3.520	330.3	10.54	2.760	218.3	10.38	2.06 ± 0.36	1.00 ± 0.26
Perseus Arm	Section 4.7	3.407	119.9	9.84	3.807	119.9	9.84	-1.69 ± 0.70	-2.11 ± 0.55

Note.
[a] A negative (positive) sign, synonymous with $h_k = -1$ (+1) in Equation (10b), indicates a CW (CCW) magnetic field, as seen from north Galactic pole. In all cases, the field is modeled as pointing parallel to the outer spiral boundary of the region.

We call this procedure the "arm-by-arm" technique, since the procedure splits the LOS quantities outward from Earth into contributions from each such zone.

Given our new RM values, we focus our magnetic field analyses on Arecibo-accessible spiral arm zones, interarm zones, and adjoining regions. In particular, we focus on parts of the Local, Carina–Sagittarius, Crux–Scutum, and Perseus Arms plus distinguishable regions between them. We searched these regions and their vicinities for systematic patterns of magnetic fields, guided partly by the results of the earlier J. M. Weisberg et al. (2004) Arecibo RM survey and also by subsequent work. We do not comment on the magnetic field structure elsewhere in the Galaxy since we have no new information to contribute in those regions. Interested readers are directed to J. L. Han et al. (2018) and J. Xu et al. (2022) for recent analyses of other zones. Those authors and most others investigating the overall structure of the Galactic plane magnetic field conclude that it lies parallel or antiparallel to spiral structures, often reversing between them and perhaps even between arm and interarm zones. However, the field direction (and magnitude) between reversals, along with the number of reversals, is still controversial.

As a first approximation to the more complicated reality, we model the form of each arm and relevant interarm region as having a constant magnetic field magnitude $|B|$ throughout, pointing either clockwise (CW, helicity $h = -1$) or counterclockwise (CCW, helicity $h = +1$) along the arm or interarm region, bounded on its Galactocentric inner and outer edges by logarithmic spirals.[8] For our equation of Galactocentric radius R as a function of Galactocentric azimuth ϕ for the ith logarithmic spiral inner or outer boundary, we follow Equation (10) in YMW17:

$$\ln \frac{R}{R_{0,i}} = (\phi - \phi_{0,i}) \tan \psi_i, \tag{4}$$

where $R_{0,i}$ is the Galactocentric radius of the ith spiral boundary at Galactocentric azimuth $\phi_{0,i}$, and ψ_i is the ith spiral pitch angle.

In concert with our zeroth-order assumption of constant field magnitude along the arm, we adjust the inner and outer edges of each such zone from their nominal locations so as to maximize the consistency of the magnetic field within the zone. The parameters of the resulting inner and outer boundaries for each zone are listed in Table 1, and those boundaries are delineated by dotted black curves in face-on Galactic plots located in or near the section discussing each zone.

Given the path integral nature of the basic observables $\mathrm{RM_{PSR}}$ and $\mathrm{DM_{PSR}}$, it is useful to break the total paths of Equations (1) and (2) into convenient subpaths, corresponding to the k distinguishable arms and interarm regions along the LOS from the jth pulsar:

$$\mathrm{RM_{PSR}}_j = \sum_{i=1}^{k} \delta \mathrm{RM}_{i,j} \ \ \mathrm{rad\ m^{-2}} \tag{5}$$

and

$$\mathrm{DM_{PSR}}_j = \sum_{i=1}^{k} \delta \mathrm{DM}_{i,j} \ \ \mathrm{pc\ cm^{-3}}. \tag{6}$$

Since the LOS from one zone may pierce other zones, we will need to adequately model the magnetic and electron density properties of the $i = 1, 2, 3, \ldots, k-1$ intervening zone(s) in order to isolate the desired properties in the target (kth) zone. This principle also dictates the order of analysis of the zones. Therefore, in the above two equations, the first subpath corresponds to the Local Arm within which we are embedded, higher-numbered ones represent successively farther zones along the LOS from Earth, and the final, kth term corresponds to the farthest subpath, which is bounded by the pulsar and the Earthward edge of the zone within which it lies.[9] This last term, the contribution of the farthest zone, can then be isolated by subtracting the already-modeled contributions of all $k-1$ intervening zones along the jth pulsar's LOS (unless the pulsar lies in the Local Arm, in which case there are no intervening zones and $k \equiv 1$):

$$\delta \mathrm{RM}_{j,k} = \mathrm{RM_{PSR},}_j - \sum_{i=1}^{k-1} \delta \mathrm{RM}_{i,j} \ \mathrm{rad\ m^{-2}} \tag{7}$$

and

$$\delta \mathrm{DM}_{j,k} = \mathrm{DM_{PSR},}_j - \sum_{i=1}^{k-1} \delta \mathrm{DM}_{i,j} \ \ \mathrm{pc\ cm^{-3}}, \tag{8}$$

where the total $\mathrm{DM_{PSR},}_j$ and $\mathrm{RM_{PSR},}_j$ are observed and each term in the summations is modeled. We name the procedure

[8] Specifically, we model the field as being locally parallel to the outer boundary in all cases.

[9] The outward (away from Earth) ordering of the summation terms in Equations (5) and (6) always associates $i = 1$ with the Local Arm and is opposite to the inward (Earthward) direction of the RM and DM path element ds and path integrals of Equations (1) and (2) and any associated subpaths. Nevertheless, the sign of each summation term is set by the result of the associated path integral.

embodied by the above two equations the "arm-by-arm" technique.

As Equations (7) and (8) provide the means to determine $\delta\mathrm{RM}_{j,k}$ and $\delta\mathrm{DM}_{j,k}$, Equation (3) can be rearranged to yield the magnetic field magnitude $|B_k|$ in the farthest (kth) subpath along this particular (jth pulsar's) LOS:

$$|B_{j,k}| = 1.232\ \frac{\delta\mathrm{RM}_{j,k}/\cos\theta_{(B\cdot ds)_{j,k}}}{\delta\mathrm{DM}_{j,k}}\ \mu\mathrm{G}. \tag{9}$$

The numerator of the above equation, $(\delta\mathrm{RM}_{j,k}/\cos\theta_{(B\cdot ds)_{j,k}})$, will hereafter be called the "geometrically corrected $\delta\mathrm{RM}_{j,k}$."

To our knowledge, our work represents the first effort to geometrically correct all analyzed RMs, thereby enabling systematic magnetic analyses along large segments of spiral arm and interarm regions, even while $\cos\theta_{(B\cdot ds)}$ varies significantly.

In much of what follows, we deploy Equations (7)–(9) as our fundamental analysis tools on a given pulsar LOS in a particular zone. A collective version of Equation (9) that averages the contributions of all pulsar–Earth subpaths originating at pulsars in the kth zone and ending at the Earthward edge of that zone provides a mean value of the arm-aligned (or antialigned) magnetic field in that zone:

$$|\bar{B}_k| = 1.232\left(\frac{\delta\mathrm{RM}_k/\overline{\cos\theta_{(B\cdot ds)_k}}}{\delta\mathrm{DM}_k}\right)\mu\mathrm{G}, \tag{10a}$$

where the overline here represents an averaging process over all $j = 1, 2, 3,\ldots, N_k$ LOS subpaths originating in zone k, i.e., those subpaths originating from all pulsars lying in zone k. (The specific nature of the "averaging process" will be delineated below.)

However, the helicity of $\cos\theta_{(B\cdot ds)_k}$ is a priori unknown. Thus, Equation (10a) does not tell us whether the field in a given magnetic arm is CW or CCW. Let us define a CCW kth arm tangential unit vector $\hat{t}_k$. Then, $\boldsymbol{B}_k = h_k|B_k|\hat{t}_k$ with a CCW ($h_k = +1$) or CW ($h_k = -1$) helicity. We can then replace $\cos\theta_{(B\cdot ds)_k}$ with $h_k\cos\theta_{(t\cdot ds)_k}$ such that we can solve for both the magnitude ($|\bar{B}_k|$) and helicity (h_k) of the magnetic field in a given zone, e.g.,

$$h_k\ \ |\bar{B}_k| = 1.232\left(\frac{\delta\mathrm{RM}_k/\overline{\cos\theta_{(t\cdot ds)_k}}}{\delta\mathrm{DM}_k}\right)\mu\mathrm{G}. \tag{10b}$$

Under our working assumption that the magnetic field magnitude $|B|_{j,k}$ is approximately constant in zone k for all $j = 1, 2, 3,\ldots, N_k$ pulsar LOSs originating in the zone, Equation (9) indicates that there will be a linear relationship between the geometrically corrected $\delta\mathrm{RM}_{j,k}$ and $\delta\mathrm{DM}_{j,k}$. We therefore create N_k ordered pairs, $z_{j,k}$, of such denominators and numerators for zone k, where

$$z_{j,k} = (\delta\mathrm{DM}_{j,\mathrm{k}},\ \ \delta\mathrm{RM}_{j,\mathrm{k}}/\cos\theta_{(B\cdot ds)_{j,\mathrm{k}}}), \tag{11}$$

with $j = 1, 2, 3,\ldots, N_k$. Our adopted "averaging process" for determining $|\bar{B}_k|$, the mean magnetic field magnitude in the kth zone, takes advantage of this linear relationship by fitting a best slope to the set of N_k pulsars' $z_{j,k}$ within the kth region and then substituting that best slope for the overlined quantities in Equations (10a) and (10b). In the fit, we do not weight each $z_{j,k}$ by its observational uncertainties, since spatial fluctuations in the interstellar medium itself induce RM variations of unknown amplitude that tend to be significantly larger than instrumentally induced RM uncertainties (H. Ohno & S. Shibata 1993; X. H. Sun et al. 2008). Instead, we weight each $z_{i,k}$ equally in the fit after rejecting $N_{k,r}$ LOSs, which represent extreme versions of the local variation phenomenon, nonphysical (negative) δDMs, or LOSs almost perpendicular to the arm.[10]

We graphically depict this zone-averaging process for each region in a so-called "ramp plot," where, for the selected (kth) zone, we display the N_k values of $z_{i,k}$ within that zone along with the line that best fits all of them. Furthermore, as indicated by Equation (10b), the direction of the field is also revealed by the ramp plot: a CCW field along the arm would result in the best-fitting line having a positive slope, whereas a CW field would lead to a negative slope.

We apply a bootstrap process (B. Efron & R. Tibshirani 1991) to estimate a first-order uncertainty in the fitted slope and in the resulting mean B-field for the arm.[11] For each such zone except the Local Arm, an additional uncertainty due to the covariance of the resulting slope with other arms' slopes was calculated and included in our error budget.[12] The additional term was negligible in all cases except that of the Perseus Arm, but it is nevertheless included in all B-field uncertainties reported in this paper.

Note that while Equations (7)–(11), as displayed, will reveal properties of the farthest (kth) zone from Earth, similar versions can be deployed to study nearer zones; indeed, the farther zones can only be studied after the nearer zones have been evaluated and modeled, as the near-zone RM and DM contributions must be subtracted from the observed values to yield the farthest zones' portions (see Equations (7) and (8), respectively). We use the YMW17 electron density model to calculate the $\delta\mathrm{DM}_i$ for any ith subpath along the LOS via a subpath piece of Equation (2). However, there does not yet exist a reliable global magnetic field model that would enable us to perform a similar $\delta\mathrm{RM}_i$ calculation with Equation (1). Instead, we develop our own model of the systematic magnetic field in a kth zone by solving for the intervening zone's $\boldsymbol{B}_i$ and hence associated $\delta\mathrm{RM}_i = \int_i n_e\boldsymbol{B}_i\cdot d\mathbf{s}/1.232$. We then apply Equation (7) to find the portion of the observed RM attributable to the farthest (kth) subpath from Earth.

This zone-by-zone procedure allows us to optimize our fit for the magnetic zone's width and field strength in each arm or interarm region independently (see Table 1 for a list of these quantities). To our knowledge, this procedure has not been used before. In principle, it can be extended in the future to additional zones as new RM measurements become available.

While our assumptions of a constant field within a zone pointing parallel to its outer boundary are inevitably over-simplified, we will show that existing pulsar RM and DM measurements are consistent with these assumptions in most cases. Specifically, our magnetic field measurements along individual LOSs through a specific arm or interarm region, calculated via Equation (9), are generally consonant with our measured average fields therein, as calculated from Equations (10a) and (10b) and the fits to N_k sets of $z_{j,k}$. However, we should also note that the random fields tend to have magnitudes comparable to or even larger than those of the systematic ones studied here that could contribute to our measured

[10] The nonphysical, negative δDMs are solely due to the selected gridding for the spiral arms.

[11] For the remainder of this work, all referred to B-fields have been geometrically corrected according to Equation (10b).

[12] The Local Arm is excluded from this analysis since there are no nearer arms to influence its LOS.

RMs (H. Ohno & S. Shibata 1993; X. H. Sun et al. 2008). This could lead to significant jitter in the RMs for a given arm.

4. Systematic Magnetic Fields in the Galactic Plane

The next sections apply our new technique to various spiral arm zones. We first investigate the Local Arm, where we illustrate our analysis techniques in some detail. We then move farther away from Earth—first to zones successively closer to the Galactic center (the Carina–Sagittarius Arm, the Sagittarius-to-Scutum Interarm region, and the Crux–Scutum Arm), and then outward to the Perseus Arm. While we also have some new RMs in the Norma-Outer Arm region, they are not sufficiently densely placed for us to detect systematic magnetic field trends there. Therefore, delineation of the Norma-Outer Arm will be deferred to future analysis.

4.1. Local Arm

While the locations and pitch angles of most spiral arms are fairly well agreed on, there is still some disagreement on these parameters for the Local Arm. Consequently, much recent work on Galactic structure has focused on this arm. The YMW17 Local Arm Center, shown as a dashed red curve in many figures in our work, uses the parameters of the L. G. Hou & J. L. Han (2014) third "4 + Local" Arm model that was fitted to H II regions. Their Local Arm presents as an angling bridge between the Carina–Sagittarius and Perseus Arms.

The resulting Local Arm has a much lower putative pitch angle than that of the other spiral arms. However, a growing body of VLBI and Gaia parallaxes (e.g., Y. Xu et al. 2013; M. J. Reid et al. 2016; Y. Xu et al. 2018; M. J. Reid et al. 2019) and a statistical study of various spiral tracers (E. Griv et al. 2017) argue for a Local Arm pitch angle similar to that of most other arms, such that the Local Arm is approximately parallel to its adjacent Carina–Sagittarius and Perseus Arms.

We therefore define the Local Arm as the region lying between the outer boundary of the Carina–Sagittarius Arm and the inner boundary of the Perseus Arm, still extending azimuthally over the approximate range of the red dashed YMW17 Local Arm and capped at both ends by lines of constant Galactocentric azimuth. It is replaced off its low-longitude end by a Perseus-to-Sagittarius Interarm region (see Section 4.6). We model the Local Arm's magnetic field to point parallel to its newly defined outer boundary, rather than to the YMW17 Local Arm center. For all these reasons, the YMW17 Local Arm center is shown as a dashed curve wherever it appears in our figures.

We adjusted the Local Arm's Galactocentric inner and outer edges until they encompassed a zone of roughly constant magnetic field directed along the arm, while simultaneously excluding zones of significantly different magnetic field. See Table 1 for the parameters of our adopted magnetic inner and outer Galactocentric boundaries for the Local Arm. In Figure 2, we illustrate the Galactic plane locations and measured RMs of all pulsars having measured values in the above-defined Local Arm region, except for those pulsars that lie within or beyond the Gum Nebula.[13]

[13] For these purposes, we adopt the YMW17 model of the location and size of the Gum Nebula—an ellipsoidal shell with its long axis oriented perpendicular to the Galactic plane, centered at a distance of 450 pc from Earth, toward $(l, b) = (264°, -4°)$, with a radius of 126.4 pc in the plane parallel to the Galactic plane that contains the center of the nebula.

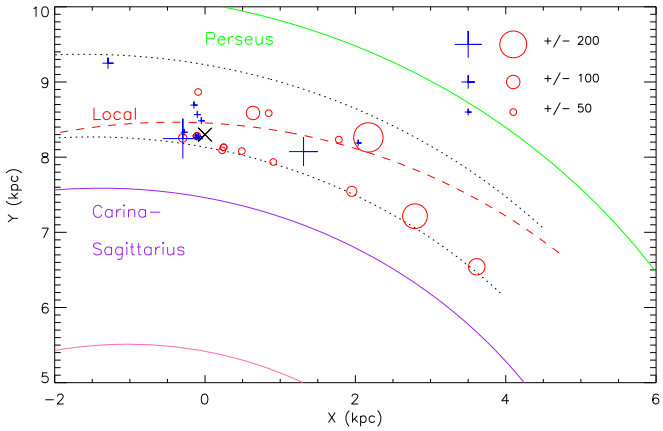

Figure 2. Measured RM_{PSR} of each low-latitude pulsar in our sample in the Local Arm region, except those in and beyond the Gum Nebula. The black dotted curves delineate the nominal inner and outer boundaries of the (magnetic) Local Arm derived from our analyses. A Perseus-to-Sagittarius Interarm region (not shown) is presumed to extend below the low-longitude end of the Local Arm (see Section 4.6). We model the magnetic field within the Local Arm to be parallel to our Local Arm's outer boundary. The black cross at $(x, y) = (0.0, 8.3)$ marks the location of the solar system.

The Gum Nebula serves as a major localized perturbation to the DMs and RMs of pulsars located in or beyond it. While C. R. Purcell et al. (2015) have created a model of the magnetic field in and near the nebula itself, its uncertainties suggest that it is best to remove pulsars in and beyond this region from our study of the Galactic magnetic field, rather than attempting to use a poorly constrained magnetic model of the Gum Nebula to calculate its contributions to larger-scale fields. The pulsars removed for this reason from Figure 2 and from our magnetic field fits are listed in Table A1.

It is important to note that the Gum Nebula lies in a complicated region of the sky, which has led other investigators (e.g., J. Xu & J. L. Han 2019) to create rather different models of its distance, size, and even shape from those of C. R. Purcell et al. (2015) and YMW17. Any of these alternate models, if adopted, would in turn lead to a somewhat different "Gum shadow zone of exclusion" and resulting set of rejected pulsars.

In Figure 3, we plot the geometrically corrected δRM_{Local} as a function of δDM_{Local} for all pulsars in the Local Arm, along with the resulting unweighted linear fit. We exclude from our fit pulsar LOSs with extreme values of $\delta RM_{Loc}/\cos\theta$, δDM_{Loc}, or B_{Loc}. Table 2 presents the rejection thresholds for each of these quantities in this arm and all successively analyzed zones, while Table 3 lists all "outlier" LOSs thereby rejected from each zone's fit and the rationale for so doing.

We find a 2σ–3σ difference in the respective linear fits for pulsars below and above the Galactic plane, and hence Figure 3 is split into two panels: one for negative Galactic latitude pulsars, and another for those at positive Galactic latitudes. For negative (positive) Galactic latitudes, the slope of the best-fit line is -2.0 ± 0.3 (-1.0 ± 0.5), which implies a magnetic field of magnitude 2.5 ± 0.4 (1.3 ± 0.6) μG, pointing CW and parallel to the arm's outer boundary.

We also study the Local Arm's magnetic field along individual pulsar LOSs as a function of both longitude and latitude. Other than a difference above and below the Galactic plane consonant with the associated RM difference noted above, we do not find any other features that depend on longitude or latitude in this region.

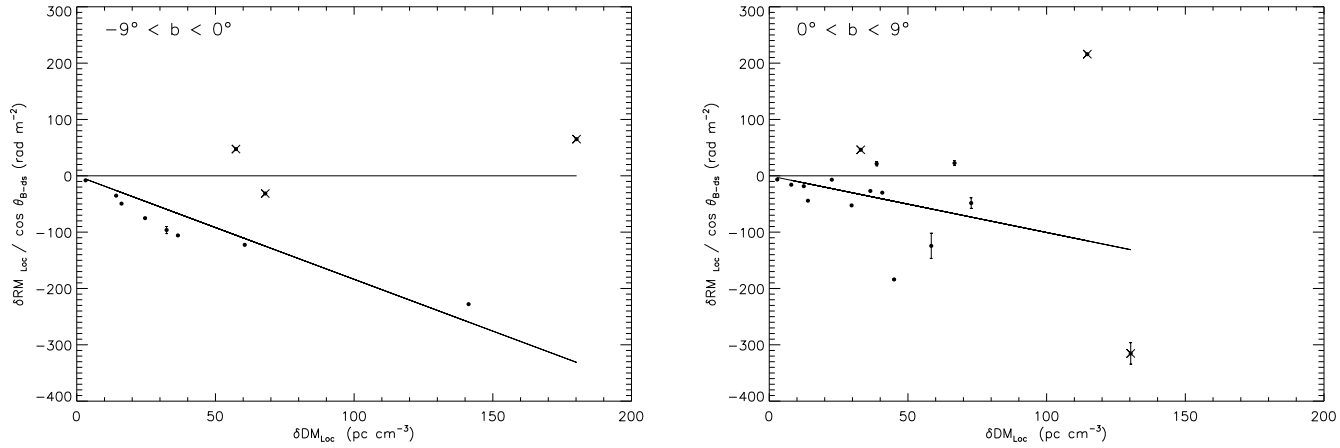

Figure 3. Left: geometrically corrected $\delta\mathrm{RM}_{\mathrm{Local}}$ as a function of $\delta\mathrm{DM}_{\mathrm{Local}}$ for the Local Arm pulsars shown in Figure 2 with negative Galactic latitudes. Right: same as the left panel, but for pulsars with positive Galactic latitudes. In each case, we show the best linear fit to the respective values. Outliers are shown with crosses, with details listed in Table 3.

Table 2
Outlier $\delta\mathrm{RM}/\cos\theta$, $\delta\mathrm{DM}$, and B Thresholds by Zone

Fitted Zone	$\delta\mathrm{RM}_{\mathrm{zone}}/\cos\theta$ Outlier Threshold (rad m^{-2})		$\delta\mathrm{DM}_{\mathrm{zone}}$ Outlier Threshold (pc cm^{-3})	B Outlier Threshold (μG)	
	Lower	Upper	Upper	Lower	Upper
Local Arm (S)	−300	200	…	−5.0	−1.0
Local Arm (N)	−300	200	…	−6.0	1.5
Sagittarius Arm (S)	−880	600	…	−3.0	9.0
Sagittarius Arm (N)	−880	600	…	−5.0	10.0
Sagittarius-to-Scutum Interarm (S)	−200	400	…	−10.0	18.0
Sagittarius-to-Scutum Interarm (N)	−400	400	400	−10.0	18.0
Scutum Arm (S)	−125	1000	…	−8.0	20.0
Scutum Arm (N)	−300	630	…	−8.0	15.0
Perseus Arm (S)	−500	500	…	−20.0	20.0
Perseus Arm (N)	−500	500	300	−20.0	8.0

To our knowledge, this work is the first that indicates a distinction between the Local Arm disk's magnetic field strength at positive and negative Galactic latitudes, albeit only at the 2σ–3σ level. A similar north–south asymmetry has been noted in the Sagittarius Arm (A. Ordog et al. 2017; Y. K. Ma et al. 2020), and indeed we find such asymmetries in most zones that we analyze in this work. See Section 5.2.3 for further discussion of the north–south asymmetries.

A CW magnetic field within the Local Arm has been well documented within the literature, with most recent investigators also suggesting that it points parallel to the nearby major arms, rather than having the anomalous pitch angle of the YMW17 model's Local Arm. There are also several estimates of the field magnitude, starting with R. N. Manchester (1972), who used pulsar RMs to infer a local field of $\sim$3.5 μG, directed toward $\ell \sim 90°$. X. H. Sun et al. (2008), using a wide variety of radioastronomical measurements but no pulsar RMs, modeled the Local Arm parallel to the nearby major arms and found that the magnetic field magnitude is $\sim$2 μG.

Most recently, J. Xu et al. (2022) fitted straight lines to sets of pulsars' total RMs as a function of pulsar distance in low latitude, $\sim$6° longitude wedges in the first Galactic quadrant, deriving LOS field strengths where possible. The wedges most comparable to ours are those of $62° < l < 70°$ and $80° < l < 90°$, as they include pulsars in the Local Arm. They find LOS magnetic field magnitudes of 1.9 ± 0.7 μG and 2.8 ± 0.6 μG, respectively, for the two ranges. As illustrated by our Equation (9), these values should be geometrically corrected in order to yield field magnitudes along the Local Arm rather than along the LOS. This correction would boost the field strength by $\sim$10% for the lower-longitude wedge and by a negligible amount for the higher-longitude one. Note that, unlike our arm-specific fits, their longitude wedge fits only incorporate RMs over relatively narrow longitude ranges. The error bars on their two Local Arm fits (after geometrical correction) plus ours all overlap.

4.2. Local-to-Sagittarius and Local-to-Perseus Interarm Regions

Our modeling, combined with the somewhat limited number of pulsar RMs within the Local-to-Sagittarius and Local-to-Perseus interarm regions, indicates no current need for distinctive field configurations (e.g., nulls, additional reversals, or significantly different magnitudes) in these zones. Consequently, we modeled the Local Arm as directly abutting the Sagittarius and Perseus Arms.

4.3. Sagittarius(–Carina) Arm

Since the Arecibo telescope could access major portions of this arm in the first Galactic quadrant (defined as $0° \leqslant \ell \leqslant 90°$) but not in the fourth, we study only the Carina–Sagittarius Arm pulsar LOS lying in the first quadrant, where the arm is called merely the Sagittarius Arm. Additionally, we eliminate the Sagittarius Arm pulsars lying below the dotted–dashed line in Figure 4 (i.e., those whose LOSs intersect the Sagittarius-to-Scutum Interarm region along the path to Earth) since the determination of the interarm magnetic properties itself depends on the magnetic properties of the Sagittarius Arm, thereby creating a situation in which the two zones' inferred magnetic properties would depend on each other.

Table 3
Pulsar LOSs Rejected as Outliers from Zonal Magnetic Field Fits

PSR	l (deg)	b (deg)	Distance (kpc)	$\delta \mathrm{RM}_{\mathrm{zone}}/\cos\theta$[a] (rad m^{-2})	$\delta \mathrm{DM}_{\mathrm{zone}}$[a] (pc cm^{-3})	B[a] (μG)	Rejection Criterion[b]
				Local Arm			
B0833−45	263.6	−2.8	0.3	−31.4	68.0	−0.6	4
B0923−58	278.4	−5.6	0.1	47.4	57.4	1.0	4
B0940−55	278.6	−2.2	0.3	65.1	180.2	0.4	4
B0959−54	280.2	0.1	0.3	−315.3	130.3	−3.0	2
B2022+50	86.9	7.5	2.1	46.2	33.0	1.7	4
J2032+4127	80.2	1.0	1.3	215.8	114.7	2.3	2, 4
				Sagittarius Arm			
B1749−28	1.5	−1.0	0.2	468.5	48.1	12.0	4
J1804−2717	3.5	−2.7	0.8	173.5	22.4	9.6	4
B1820−31	2.1	−8.3	1.6	401.9	48.0	10.3	4
J1920+1110	46.2	−1.2	6.1	660.2	177.6	4.6	2
J2017+2043	61.4	−8.3	4.2	−146.9	52.0	−3.5	4
J2015+2524	65.0	−5.3	0.9	−8.1	1.5	−6.9	4
J2016+1948	60.5	−8.7	2.2	−108.1	25.8	−5.2	4
J1730−2304	3.1	6.0	0.6	−34.2	7.3	−5.8	4
J1802−2124	8.4	0.6	0.8	854.3	147.3	7.2	2
B1822−09	21.4	1.3	0.3	131.6	9.5	17.1	4
B1907+12	46.2	1.6	8.1	1001.3	254.2	4.9	2
B1911+13	47.9	1.6	5.3	612.3	140.4	5.4	2
B1921+17	51.7	1.0	4.0	614.9	137.2	5.5	2
				Sagittarius-to-Scutum Interarm			
J1759−2922	1.2	−2.9	2.4	849.6	23.7	44.3	2, 4
B1853+01	34.6	−0.5	3.3	−217.3	15.4	−17.4	2, 4
B1854+00	34.4	−0.8	2.5	34.0	2.0	20.6	4
J1901+0254	36.6	−0.9	4.3	−206.4	99.8	−2.6	2
B1859+03	37.2	−0.6	7.0	−315.6	314.6	−1.2	2
J1907+0740	41.6	−0.1	5.8	487.1	225.1	2.7	2
B1907+03	38.6	−2.3	2.9	−214.6	1.1	−245.3	2, 4
J1910+0728	41.7	−0.8	6.2	473.0	178.7	3.3	2
J1915+0752	42.6	−1.6	3.6	122.6	4.5	33.4	4
J1832−0836	23.1	0.3	2.5	−22.6	−46.4	⋯	1
J1901+0510	38.7	0.0	5.9	1212.0	335.9	4.5	2
J1901+0621	39.7	0.8	2.9	−336.9	0.5	−831.7	4
B1900+06	39.8	0.3	7.0	463.8	406.5	1.4	2, 3
J1902+0723	40.7	1.0	3.3	−357.3	9.2	−48.2	4
B1907+10	44.8	1.0	4.8	429.5	21.2	25.0	2, 4
J1848+0826	40.2	4.4	3.9	216.6	12.8	21.0	4
				Scutum Arm			
B1758−29	1.4	−3.2	3.0	−378.3	41.3	−11.3	2, 4
B1842−04	28.2	−0.8	4.1	−379.0	73.1	−6.4	2
J1849−0614	27.2	−2.5	3.5	394.5	7.6	64.3	4
J1900−0051	33.2	−2.5	4.2	193.7	4.7	50.7	4
J1902−0340	31.0	−4.2	4.0	228.0	10.2	27.5	4
B1911−04	31.3	−7.1	4.0	−24.1	3.5	−8.5	4
B1917+00	36.5	−6.2	5.9	84.1	−18.2	⋯	1
J1858+0241	36.2	−0.4	5.2	−200.3	16.2	−15.3	2, 4
J1741−2733	0.6	1.6	3.1	−480.0	57.1	−10.4	2, 4
B1804−12	17.1	4.4	3.0	342.9	7.4	57.2	4
J1829+0000	30.5	4.8	4.3	−125.0	17.8	−8.7	4
B1834−06	25.2	0.0	4.1	−386.4	159.4	−3.0	2
J1841−0345	28.4	0.4	3.8	470.4	31.3	18.6	4
B1839−04	28.3	0.2	3.7	326.2	26.2	15.3	4
J1842−0415	28.1	0.1	3.6	−168.5	18.8	−11.1	4
B1845−01	31.3	0.0	4.4	500.0	−39.8	⋯	1
J1849+0127	34.0	1.0	4.7	−216.3	32.6	−8.2	4
J1850−0006	32.8	0.1	5.6	631.9	351.9	2.2	2
				Perseus Arm			

Table 3
(Continued)

PSR	l (deg)	b (deg)	Distance (kpc)	$\delta RM_{zone}/\cos\theta$[a] (rad m^{-2})	δDM_{zone}[a] (pc cm^{-3})	B[a] (μG)	Rejection Criterion[b]
B0329+54	145.0	−1.2	1.7	−130.7	6.5	−24.7	4
B0525+21	183.9	−6.9	1.2	264.6	9.4	34.8	4
B0531+21	184.6	−5.8	2.0	292.0	14.4	25.0	4
J0538+2817	179.7	−1.7	1.3	−164.0	0.4	−470.9	4, 5
B2035+36	76.7	−2.8	4.9	448.7	19.2	28.9	4
J0215+6218	132.6	1.0	2.0	735.8	63.2	14.4	2, 4
J0248+6021	136.9	0.7	2.0	−307.3	349.8	−1.1	3
B0355+54	148.2	0.8	1.0	268.6	36.5	9.1	4
B0450+55	152.6	7.5	1.2	47.2	−6.5	0.0	1
B0458+46	160.4	3.1	1.3	−1267.2	17.4	−89.8	2, 4, 5
J0611+30	181.6	5.5	1.1	−31.3	4.4	−8.7	5
J0709+0458	210.5	6.2	1.2	−25.2	0.7	−44.0	4
J0540+3207	176.7	0.8	1.4	−74.8	25.4	−3.6	5
J0711+0931	206.7	8.8	1.2	−63.0	1.1	−73.5	4

Notes.
[a] The given quantity refers to the value associated with the specified arm or interarm region.
[b] Rejection criteria: 1: negative δDM; 2: $\delta(\mathrm{RM}/\cos\theta)$ outlier; 3: δDM outlier; 4: B outlier; 5: $\boldsymbol{B} \perp \boldsymbol{ds}$ (i.e.,$|\cos\theta| < 0.2$).

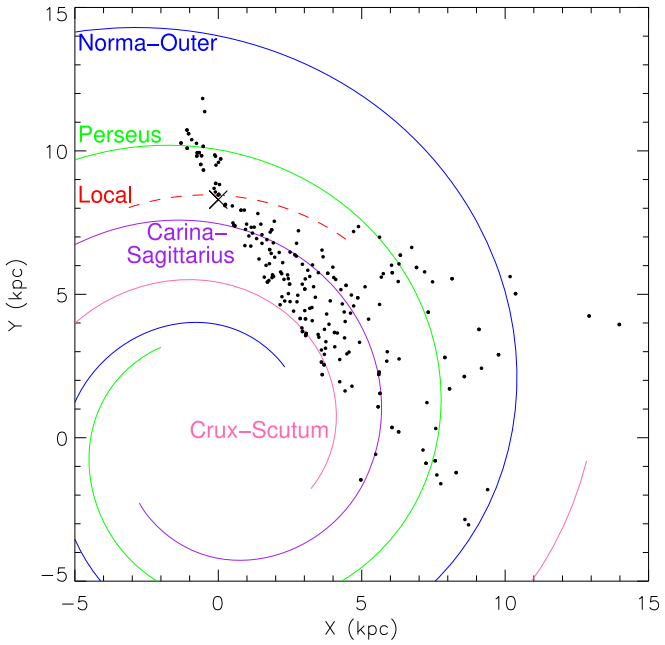

Figure 4. Same as Figure 2, but for the Sagittarius Arm. The dotted–dashed line represents the Galactic longitude limit below which the LOS would also sample the next inward region, the Sagittarius-to-Scutum Interarm.

As explained above in Section 4.2, the Galactocentric outer edge of the Sagittarius Arm is identical to the Galactocentric inner edge of the Local Arm. For the Sagittarius Galactocentric inner arm boundary, we followed the same procedure as that for the Local Arm, adjusting the boundary until the Sagittarius Arm encompassed a zone of roughly constant magnetic field directed along the arm. See Table 1 for the parameters of our adopted inner and outer Sagittarius Arm boundaries. All pulsars meeting the above criteria, as well as their measured total RMs, are shown in Figure 4.

The Sagittarius Arm components of geometrically corrected δRM and of δDM for each of these pulsars were calculated from Equations (7) and (8), respectively, so as to remove the Local Arm contributions to the observed total quantities $\mathrm{RM_{PSR}}$ and $\mathrm{DM_{PSR}}$. Given that we found different slopes and hence different magnetic fields in the intervening positive- versus negative-latitude Local Arm LOS, we also split the Sagittarius Arm's geometrically corrected δRMs and δDMs into positive and negative Galactic latitude sets. In Figure 5, we show the geometrically corrected $\delta\mathrm{RM_{Sag}}$ as a function of $\delta\mathrm{DM_{Sag}}$ and the resulting unweighted linear fit to these two data sets. Under our working assumption that the magnetic field magnitude in the Sagittarius Arm is constant and directed parallel or antiparallel to it, we use Equation (10b) to solve for the magnitude and direction of B_{Sag} along the specified fitted region of the arm.

The resulting best-fit slope for negative (positive) Galactic latitude pulsars in the Sagittarius Arm is 0.3 ± 0.3 (1.5 ± 0.2), which implies a magnetic field strength of 0.3 ± 0.3 (1.9 ± 0.2) μG, both pointing in the CCW direction along the arm. We note that our negative Galactic latitude fit, while significantly different from the positive-latitude value, is not statistically different from zero. There are several plausible explanations—e.g., the random or locally perturbed magnetic field might dominate here over its systematic component (H. Ohno & S. Shibata 1993; X. H. Sun et al. 2008), our model might not properly describe the overall magnetic field in this region (see, e.g., our evidence in Section 5.3.2 for a field reversal between the inner and outer Galactocentric boundaries of the arm itself), or the number of measurements is simply inadequate to achieve statistical significance among the fluctuations (which implies that additional measurements might permit a more robust fit).

The difference between our δRMs above and below the plane in the Sagittarius Arm is also visible in Figure 6, where we show the Sagittarius Arm B-fields determined from individual pulsar LOSs as a function of Galactic latitude. A north–south asymmetry (in both the Local and Sagittarius Arms) is echoed in previous Galactic synchrotron emission and total RM or Faraday depth (FD)[14] measurements of pulsars and EGSs in these directions (A. Ordog et al. 2017;[15] Y. K. Ma

[14] In the simplest cases, RMs and FDs are identical.
[15] These results will be further detailed in Section 5.3.2.

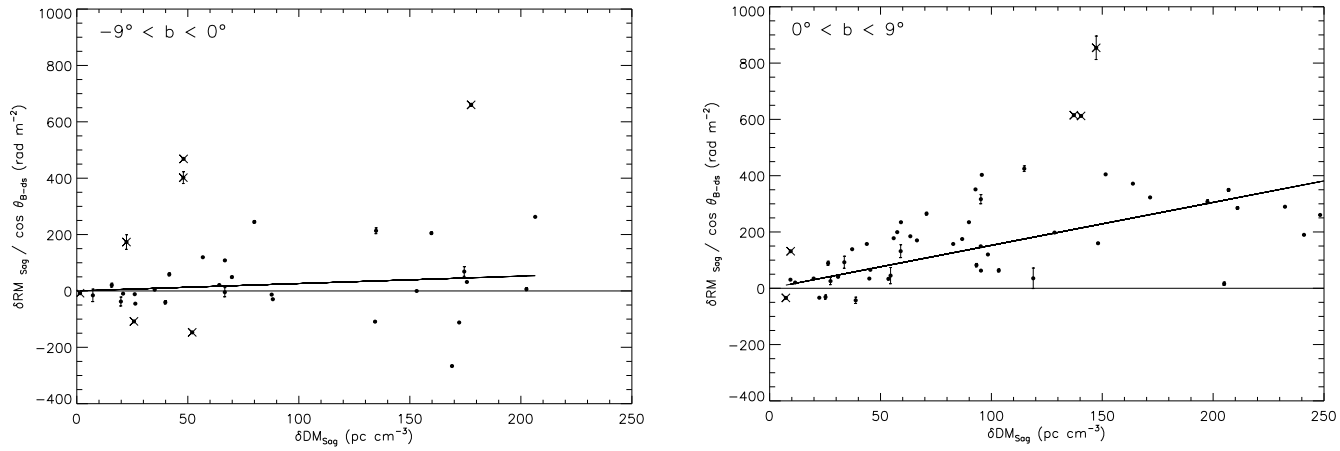

Figure 5. Same as Figure 3, but for pulsars in the Sagittarius Arm.

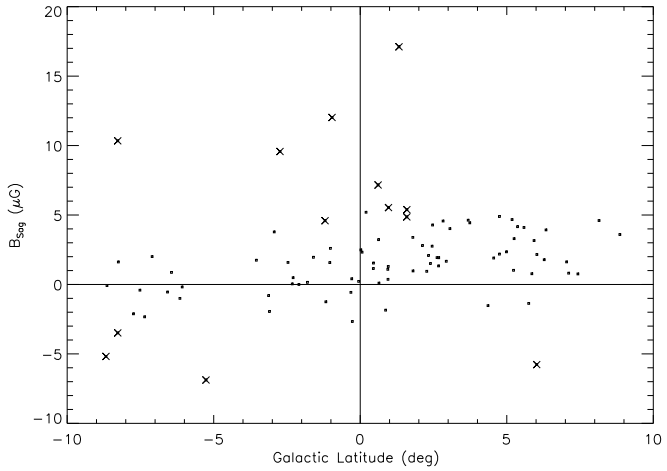

Figure 6. Derived longitudinal magnetic field strengths (positive is CCW) along our Sagittarius Arm zone as a function of Galactic latitude. Outliers are denoted with a cross and listed in Table 3.

et al. 2020). The latter reference attributed differences in the RM and magnetic field above and below the plane in the longitude region of $35° < l < 50°$ to an odd z-parity field within the disk along the Sagittarius Arm. We discuss this asymmetry in more detail in Section 5.3.2 in the context of the field reversal inside the solar circle.

J. L. Han et al. (2018) and J. Xu et al. (2022) also studied sections of the low-latitude Sagittarius Arm that we analyzed. Their field estimation technique was reminiscent of ours, in that they fitted a straight line to RM as a function of DM for a set of pulsars. However, unlike our procedure, they used the total observed RM and DM rather than first extracting only the Sagittarius Arm component. They also did not geometrically correct the RMs. These issues were partly ameliorated by their confining each of their analyses to the set of pulsars lying within a relatively narrow longitude wedge of the Galactic plane (e.g., the longitude wedges discussed in Section 4.1), rather than attempting a fit to all pulsars within a significantly longer region of an arm as we do.

J. L. Han et al. (2018) found a magnetic field strength of 1.4 ± 1.0 μG in the Sagittarius Arm over the longitude range of 45°–60° between 3 and 8.5 kpc from Earth, where the LOS traverses the Sagittarius Arm over relatively long distances. Despite the above-noted limitations on their technique, their (relatively large) error bar overlaps those of our north and south fits.

None of the three low Galactic latitude Sagittarius Arm longitude wedges studied by J. Xu et al. (2022) correspond well to the long Sagittarius Arm segment considered in this work, so direct comparison of our calculated Sagittarius magnetic field with each of their fits is difficult. Nevertheless, we attempt to do so in what follows.

(i) Their "Inner Sagittarius" fit covers the region from $44° < l < 50°$ and distances ranging between 3 and 12 kpc. LOSs in this zone traverse the Sagittarius-to-Scutum Interarm region for their first 2 kpc and then obliquely cross the Sagittarius and Perseus Arms, rendering those other non–Sagittarius Arm regions partly responsible for the total RMs and DMs to which these authors fit. In addition, as they do not geometrically correct their RMs along the LOS, their resulting field values represent only the LOS component. They find a field magnitude of 3.9 ± 1.3 μG, well above either our north or south fits for the field along the arm. Additionally, as discussed below, there is a localized enhancement of the field in their sampling zone, which could also explain the discrepancy. (ii) The authors' "mid-Sagittarius" fit almost entirely samples the Perseus Arm and does not include the Sagittarius Arm. (iii) Their "outer Sagittarius" fit samples the region from $56° < l < 62°$ and distances ranging from 3 to 8.5 kpc. Only the first 2 kpc of this wedge lie in the Sagittarius Arm. Their fitted field in the "outer Sagittarius" region, 0.7 ± 0.3 μG, is more in line with the mean of our north and south fits for this arm, despite all of the differences between our fitting methods.

R. Shanahan et al. (2019, hereafter S19) studied extragalactic RMs in the $\ell = 39°$–$52°$ range near the Galactic plane, a region within our much broader (in Galactic longitude) Sagittarius Arm zone. Their techniques, unlike ours, did not (and could not) explicitly split the LOS measurements they acquired into subpaths associated with particular Galactic zones (e.g., arms or interarm regions), due to the extragalactic nature of their studied sources. It is useful to compare and contrast S19's and our results. One of their most notable findings is a sharp and strong peak in measured extragalactic-source RM at $\ell = 48° \pm 1°$, with the most extreme part extending over less than 1° of longitude where RMs range up to more than 4000 rad m^{-2}. They argue that this RM enhancement originates in material in or near the Sagittarius Arm. They also note that there is no corresponding DM increase in pulsars at those longitudes, which seems to imply (via Equation (9)) that the

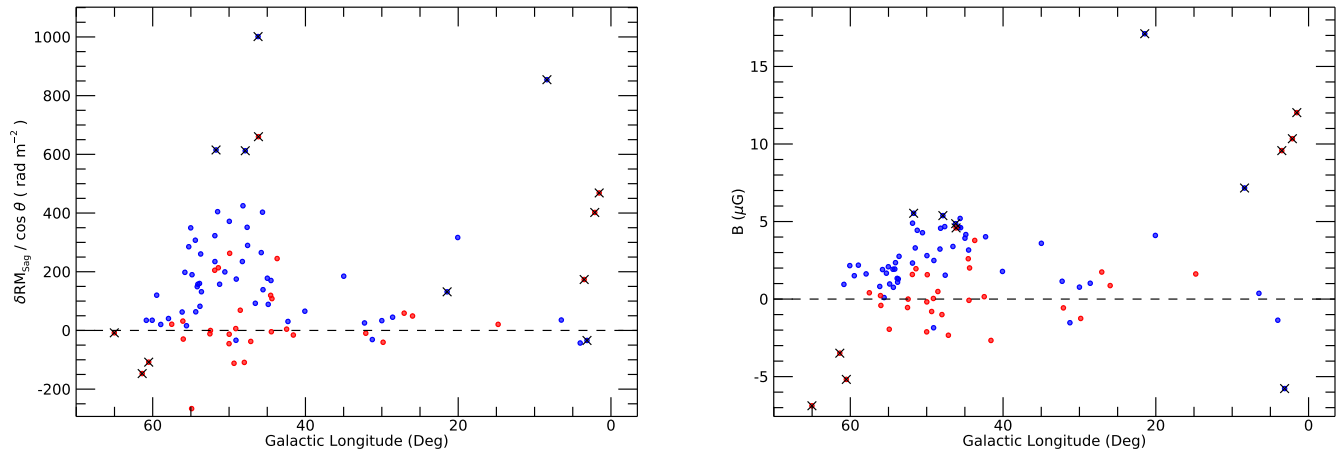

Figure 7. Left: the geometrically corrected δRM_{Sag} as a function of Galactic longitude for the Sagittarius Arm pulsars of Figure 4. Right: same as the left panel, except that the magnetic field (positive is CCW) along the arm is displayed. Pulsar LOSs at negative (nonnegative) Galactic latitudes are shown with red (blue) symbols. Outliers are denoted with a cross and listed in Table 3.

arm's magnetic field is also greatly enhanced in that region. However, we note that Equation (9) is not strictly applicable to S19's analysis for several reasons. First, the (Galactic) pulsars used by S19 are at various distances inside the Galaxy so that the associated DMs represent path integrals of various shorter lengths, whereas their extragalactic-source RMs are integrated over a much longer path. Additionally, the positions on the sky of S19's disparate RM and DM sources are not identical. In an effort to further investigate this region, we carried out two related analyses.

First, we show our geometrically corrected δRM_{Sag} as a function of Galactic longitude for the Sagittarius Arm pulsars that are shown in Figure 4 (see Figure 7, left panel). We do observe an enhanced geometrically corrected δRM_{Sag} at the longitude of the S19 RM enhancement, although ours is broader in longitude and only about a quarter of their amplitude. Since the arm's field and the LOS are essentially parallel at this longitude, our geometrical correction makes little difference and cannot explain the discrepancy. We conclude that most of the significantly larger S19 extragalactic-source RM enhancement must actually occur in regions lying beyond the Sagittarius Arm along the LOS, such as the Perseus and/or Outer Arms.

Second, for each of the pulsars that we used in our first study, we determine B_{Sag} via Equation (9) and then plot these values as a function of Galactic longitude (see Figure 7, right panel). While our measured B_{Sag} is generally enhanced by a factor of $\sim$2 in this longitude range over our measured mean value along the much larger section of arm discussed above ($0^\circ \lesssim \ell \lesssim 60^\circ$), this enhancement is much more modest than the claimed S19 RM increase. This puzzling discrepancy between the modest increase in our measured B_{Sag} and the large extragalactic-source RM enhancements of S19 has already been partially resolved above, when we showed that much of the latter enhancement must occur beyond the Sagittarius Arm. Additionally, because we can determine the geometrically corrected δRM_{Sag} and also δDM_{Sag} along an identical LOS to a given pulsar, we can deploy Equation (9) much more accurately, and we find that much of the δRM_{Sag} enhancement in the numerator of Equation (9) is usually countered by a similar (though smaller) δDM_{Sag} enhancement in the denominator, thereby moderating any increase in the quotient, B_{Sag}.

We also note that the enhancement in the geometrically corrected δRM_{Sag} around $\ell = 48^\circ \pm 1^\circ$ occurs principally at positive latitudes (Figure 7, left panel). However, our sample of negative-latitude pulsars within this region is limited, and hence a definitive conclusion cannot be made here.

It is also worth recalling that our fits for B_{Sag} (see Figure 5 and Table 1) assume and solve for a constant value along the arm, whereas the modestly enhanced B near $\ell = 50^\circ \pm 5^\circ$, especially at low positive latitudes, demonstrates that our model is an oversimplification in this region. It is beyond the scope of this work to use a more sophisticated model of the arm's magnetic field.

4.4. Sagittarius(–Carina)-to-(Crux–)Scutum Interarm Region

The interarm region between the Carina–Sagittarius Arm and the Crux–Scutum Arm is also partly visible to the Arecibo telescope. We study it throughout the first Galactic quadrant, where its name can be shortened to the Sagittarius-to-Scutum Interarm region and will be further shortened to "SSI" when used in a subscript. We define the outer Galactocentric boundary of this interarm region to be identical to the inner boundary of the Sagittarius Arm. To select the best inner boundary, we follow the same method that we used for the Sagittarius Arm in Section 4.3. Similarly to the Sagittarius Arm, we then reject pulsars lying between these inner and outer spiral boundaries whose pulsar-to-Earth LOSs cross the Scutum Arm so as to avoid a situation in which the two zones' inferred magnetic properties would depend on each other. The line demarcating this final rejection criterion is shown in Figure 8, along with our chosen inner and outer spiral-shaped boundaries. Of the remaining pulsars, we determine δDM_{SSI} and the geometrically corrected δRM_{SSI}, plotting them separately in Figure 9 for negative and positive Galactic latitude pulsars.

As illustrated in Figure 9, we find that the best-fit slope for negative (positive) Galactic latitude pulsars in the Sagittarius-to-Scutum Interarm region is $+0.8 \pm 0.2$ (-0.2 ± 0.3), which implies a magnetic field strength of 1.0 ± 0.3 (-0.3 ± 0.4) μG in the CCW (CW) direction, parallel to the outer edge of the Sagittarius-to-Scutum Interarm. While the negative-latitude fit is significant ($>3\sigma$), we note the significant scatter in δRM_{SSI} around $\delta DM_{SSI} = 0$ (see the left panel of Figure 9). This suggests that magnetic field variations near the interarm's

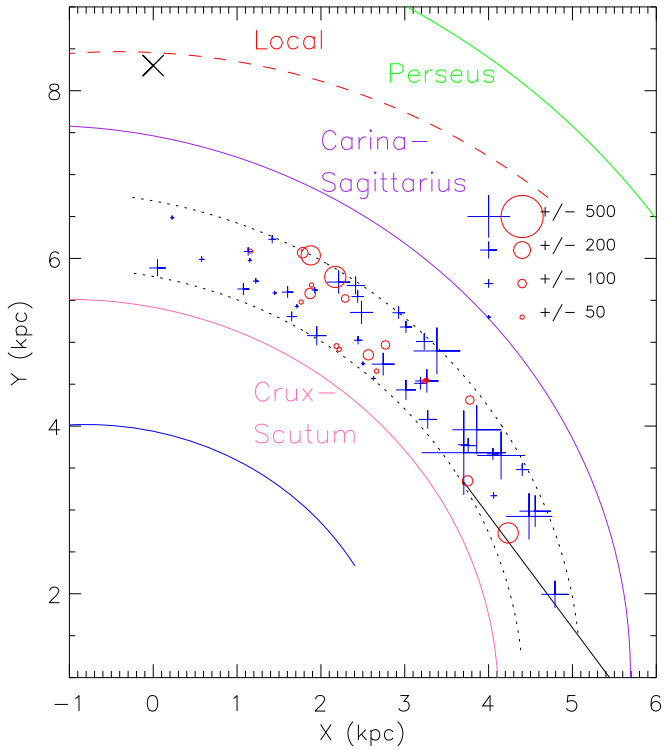

Figure 8. Same as Figure 4, but for the Sagittarius-to-Scutum Interarm region. The dotted–dashed line represents the Galactic longitude limit below which the LOS would also sample the next inward region, the Scutum Arm.

Earthward edge are larger than usual. For positive-latitude pulsars (see the right panel of Figure 9), the best-fit slope and resulting systematic magnetic field are consistent with zero, presumably for one or more of the reasons we advanced to explain a similar result for the negative-latitude Sagittarius Arm pulsars (see Section 4.3). We also study the interarm's magnetic field along individual pulsar LOSs, as a function of both longitude and latitude in this region. Similar to the Local Arm, we do not find any features other than those noted above that depend on longitude or latitude in this region.

The CCW direction of the field that we derived from negative Galactic latitude pulsars in this region agrees with the recent work of J. L. Han et al. (2018) and J. Xu et al. (2022). However, their measured magnetic field magnitudes of $3.3 \pm 0.9\ \mu$G and $3.0 \pm 0.9\ \mu$G, respectively, are significantly larger than our determinations at either negative or positive Galactic latitudes. As we also noted in our Sagittarius Arm discussion (see Section 4.3), the earlier groups' methods differed from ours in that they did not geometrically correct their RMs, nor did they constrain their fits solely to the arm in question. For example, the "Scutum−Sgr" fits of J. L. Han et al. (2018) and of J. Xu et al. (2022) sample not only the interarm region but also the zone extending 3–4 kpc beyond it, piercing both the Sagittarius and Perseus Arms. An additional fit by J. Xu et al. (2022), labeled "Inner Sagittarius," also samples the interarm region but also obliquely intersects the Sagittarius and Perseus Arms, yielding the even higher magnetic field estimate of $3.9 \pm 1.3\ \mu$G.

4.5. Scutum(–Crux) Arm

We study only that part of the Crux–Scutum Arm lying in the first Galactic quadrant, where it is called the Scutum Arm. We define the outer boundary of the Scutum Arm to be identical to the inner boundary of the Sagittarius-to-Scutum Interarm region, while we set a Galactocentric inner limit in a manner similar to our procedure for previous zones. Next, we reject pulsars lying between these inner and outer spiral boundaries whose pulsar-to-Earth LOSs cross the next inward zone. The line demarcating this final rejection criterion is shown in Figure 10, along with our chosen inner and outer arm boundaries and the locations and RMs of pulsars lying within all of these boundaries.

For the set of Scutum Arm pulsars shown in Figure 10, we calculate the geometrically corrected $\delta\mathrm{RM}_{\mathrm{Scutum}}$ as a function of $\delta\mathrm{DM}_{\mathrm{Scutum}}$ separately for both negative- and positive-latitude pulsars. We show these quantities for the negative (positive) Galactic latitude pulsars from Figure 10 in the left (right) panel of Figure 11. For negative (positive) Galactic latitude pulsars, the best-fit slope is $+1.7 \pm 0.3$ ($+0.8 \pm 0.2$), which implies a magnetic field of $+2.1 \pm 0.3 (+1.0 \pm 0.2)\ \mu$G, both pointing in the CCW direction.

While the negative-latitude fit is significant ($>6\sigma$), it appears to be dominated by four pulsar LOSs at large $\delta\mathrm{DM}_{\mathrm{Scut}}$. However, there are no indications that these four LOSs are unrepresentative, as they all originate from different longitudes and thus are not all behind a common perturber such as an H II region or magnetic bubble. Furthermore, a fit excluding these four points changes the slope by $<1\sigma$.

The fit for positive-latitude pulsars is again significant ($>4\sigma$), but it is worth noting that many of the lowest-DM points (i.e., those whose pulsar–Earth LOSs originate toward the Earthward side of the arm) tend to lie below the best-fit line. However, similar to the negative-latitude pulsars, they all originate from a range of longitudes and thus are not all behind a common perturber such as an H II region or magnetic bubble. This suggests that we did not adequately model the magnetic field prior to this arm for certain pulsar LOSs, or that we did not satisfactorily model its Earthward boundary. Additional measurements in the future should help to resolve this issue.

We study the Scutum Arm magnetic fields along individual pulsar LOSs in Figure 12. We do not find any trend with longitude for the positive-latitude LOSs. However, negative-latitude LOSs have significantly higher B at $0^\circ \lesssim \ell \lesssim 15^\circ$ than at $\ell \gtrsim 15^\circ$. The average magnetic field strength within $0^\circ \lesssim \ell \lesssim 15^\circ$ is $\sim 10\ \mu$G, significantly higher than our average fitted value.

Previous studies of the magnetic field in the Scutum Arm have found varying magnetic field magnitudes and even opposite directions. Using extragalactic sources and pulsars, C. L. Van Eck et al. (2011) found a weak CW magnetic field within this region. Later, J. L. Han et al. (2018) found a CCW magnetic field of strength $0.4 \pm 0.4\ \mu$G in the Scutum Arm in the first quadrant, a field strength consistent with zero. The more recent work by J. Xu et al. (2022) finds a nonzero CCW magnetic field in the Scutum Arm of $1.2 \pm 0.6\ \mu$G, in agreement within 1σ with our derived magnetic field both above and below the plane. However, as discussed previously, given that we employ a different technique than J. L. Han et al. (2018) and J. Xu et al. (2022), direct comparison is difficult.

4.6. Perseus-to-Sagittarius Interarm

As noted in Section 4.1, our Local Arm's low Galactic longitude limit lies at the Galactocentric azimuth of the low-longitude end of the YMW17-defined (red dashed) arm. We

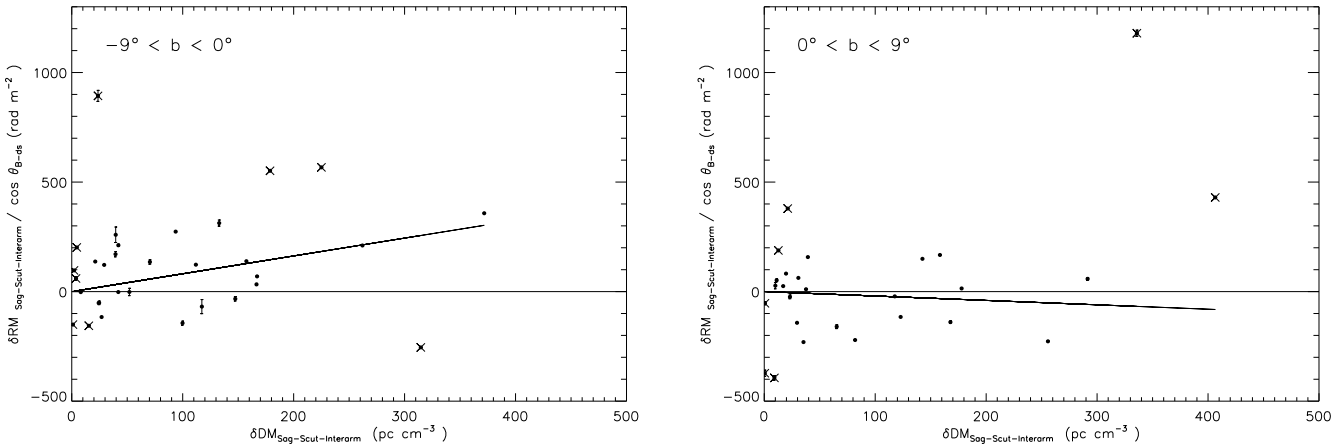

Figure 9. Same as Figure 3, but for pulsars in the Sagittarius-to-Scutum Interarm.

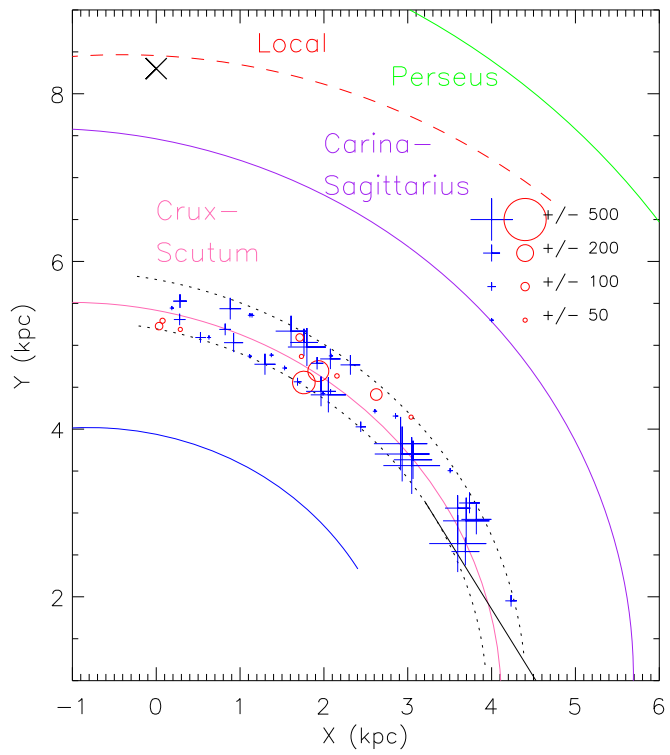

Figure 10. Same as Figure 2, but for the Scutum Arm. The dotted–dashed line represents the Galactic longitude limit below which the LOSs would also sample the next inward region.

define the Perseus-to-Sagittarius Interarm region as the extension of the Local Arm toward lower Galactic longitudes and between the upper boundary of the Sagittarius Arm (see Section 4.3) and the lower boundary of the Perseus Arm (see Section 4.7). Given the lack of pulsar RMs in our sample within the Perseus-to-Sagittarius Interarm region, we do not model the magnetic field within it.

4.7. Perseus Arm

The Arecibo telescope could access significant portions of the Perseus Arm in both the first and third Galactic quadrants. We also study this arm in the second quadrant exclusively via others' measurements, thereby linking the two Arecibo-accessible Perseus regions into a single long zone for our work.

We define the Perseus Arm center via the YMW17 model and its inner boundary to be identical to the outer boundary of the Local Arm, but extending to much higher and lower Galactic longitudes. We define the outer boundary of the Perseus Arm using the same procedure applied to previous arms. Our Perseus Arm analysis zone is truncated at both ends where pulsar LOSs pierce poorly understood intervening regions. The high-longitude limit of our analysis is set so as to avoid any LOSs sampling the magnetic field in the Gum Nebula. The low-longitude limit is set to avoid LOSs that sample the Perseus-to-Sagittarius Interarm region since we were unable to model it (see Section 4.6).

All pulsars within our Perseus Arm analysis zone are shown in Figure 13. For the set of Perseus Arm pulsars shown in Figure 13, we calculate the geometrically corrected $\delta\mathrm{RM}_{\mathrm{Perseus}}$ as a function of $\delta\mathrm{DM}_{\mathrm{Perseus}}$ separately for both negative- and positive-latitude pulsars using Equations (7) and (8). We show these quantities for the negative (positive) Galactic latitude pulsars from Figure 13 in the left (right) panel of Figure 14.

For negative (positive) latitude pulsars, the best-fit slope is -1.4 ± 0.6 (-1.7 ± 0.4), which implies a magnetic field of -1.7 ± 0.7 (-2.1 ± 0.6) μG, both pointing in the CW direction along the arm.[16] The fit for negative-latitude pulsars has a significance of 2.4σ with notable scatter about $\delta\mathrm{RM}_{\mathrm{Pers}} \sim 0$. The fit for positive-latitude pulsars is more significant (3.8σ) with relatively less scatter about $\delta\mathrm{RM}_{\mathrm{Pers}} \sim 0$. For both the negative- and positive-latitude fits, we do not find any additional evidence for a longitude or latitude dependence of the magnetic field other than that mentioned above.

In addition to the Perseus Arm regions excluded from analysis as described above, our following discussion of the Perseus Arm field must be qualified by the fact that LOSs toward it intersect a less completely sampled part of the Local Arm's magnetic field, namely those parts lying toward larger Galactocentric radii (see Section 4.1 and Figure 2 therein). Hence, our estimates of the intervening Local Arm field may not be fully representative of the LOSs toward the Perseus Arm. It will be possible to remedy this issue in the future, as more RMs in the outer regions of the Local Arm become available.

[16] As noted in Section 3, the Perseus Arm is the only zone analyzed whose covariance between two arms' fitted slopes (in this case Local and Perseus) leads to a significant enhancement of the total uncertainty.

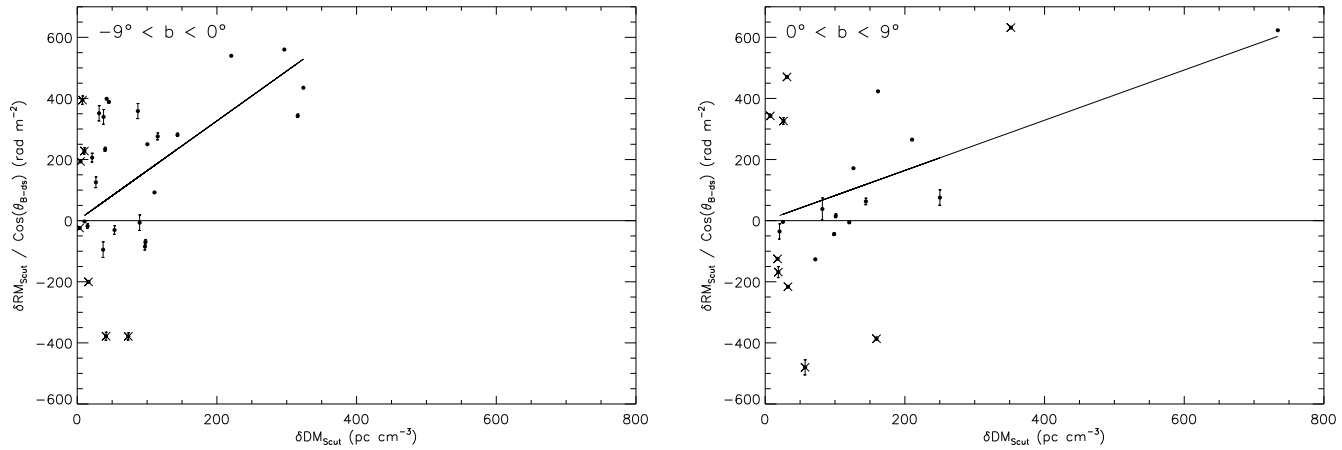

Figure 11. Same as Figure 3, but for pulsars in the Scutum Arm.

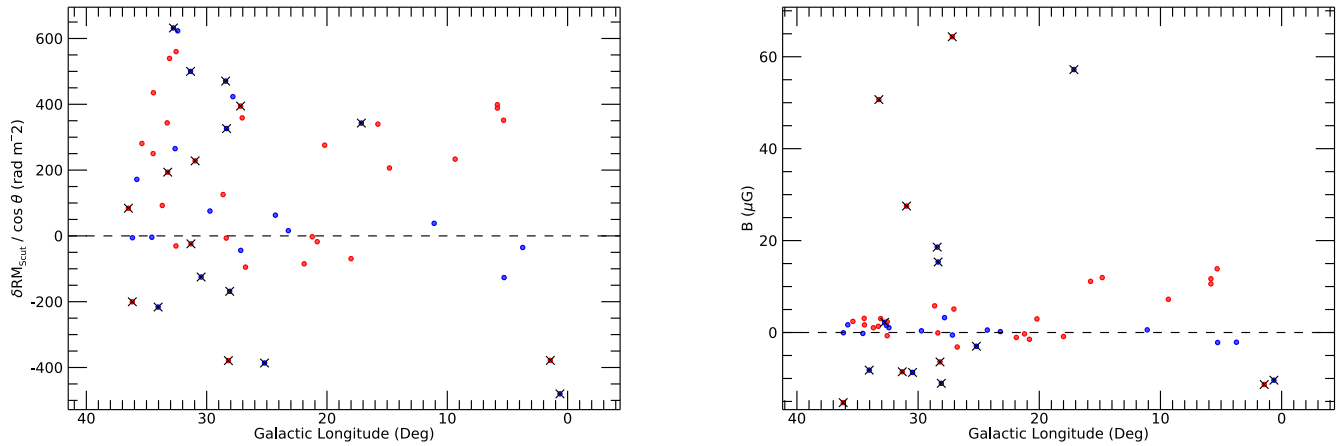

Figure 12. Left: the geometrically corrected $\delta\mathrm{RM}_{\mathrm{Scut}}$ as a function of Galactic longitude, for the Scutum Arm pulsars of Figure 11. Right: same as the left panel, except that the magnetic field B is displayed (positive is CCW) along the Scutum Arm. Pulsar LOSs at negative (nonnegative) Galactic latitudes are shown with red (blue) symbols. Outliers are denoted with a cross and listed in Table 4.

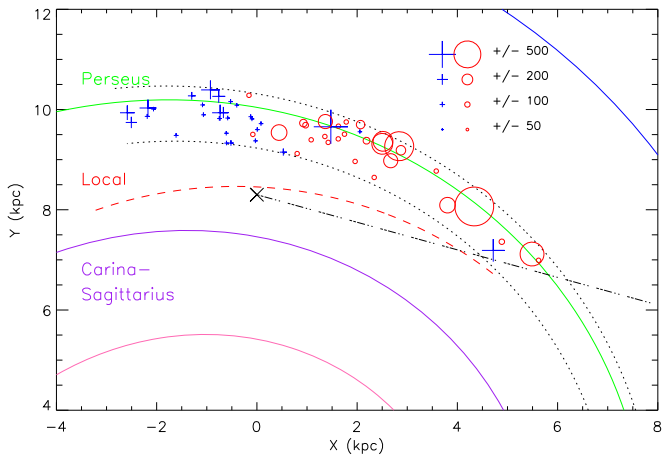

Figure 13. Same as Figure 2, but for the Perseus Arm. The dotted–dashed line represents the Galactic longitude limit below which the LOS would also sample the Sagittarius-to-Perseus Interarm.

A CW magnetic field within the Perseus Arm is similar to that found by D. Mitra et al. (2003) and C. L. Van Eck et al. (2011). Using RMs from 11 pulsars along the direction of the Perseus Arm, D. Mitra et al. (2003) determine a CW magnetic field with magnitude $-1.7 \pm 1.0\ \mu$G. This is in agreement with both our negative and positive Galactic latitude magnetic field derivations for the Perseus Arm. C. L. Van Eck et al. (2011) use EGS measurements and also find a CW magnetic field for the Perseus Arm. However, C. L. Van Eck et al. (2011) find that while the magnetic field tends to follow the spiral arms in the inner Galaxy, it is largely azimuthal in the outer Galaxy (where the outer Galaxy is defined as that part lying outside of the Local Arm). Thus, C. L. Van Eck et al. (2011) do not provide a field strength for the Perseus Arm alone. We note that the Perseus Arm is largely contained within region 5C of their Figure 6, for which the magnetic field strength is -0.86 ± 0.09 at $R = 8.5$ kpc and decreases as a function of R^{-1}.

Unlike the CW field determination of D. Mitra et al. (2003), C. L. Van Eck et al. (2011), and the current work, J. M. Weisberg et al. (2004) and J. L. Han et al. (2018) both attribute a CCW magnetic field to the Perseus Arm. J. M. Weisberg et al. (2004) model the Perseus Arm using a small sample of pulsars within the large longitude range of 60°–78°. While their sample is limited to eight pulsars, they find two field reversals in this longitude region: one at $d \sim 4.5 \pm 1$ kpc and one at $d \gtrsim 6$ kpc (see their Figure 9). Similarly, J. L. Han et al. (2018) find an increase in pulsar RMs for distances >5 kpc in the longitude region of $60° < l < 80°$. However, the longitude region used in both J. M. Weisberg et al. (2004) and J. L. Han et al. (2018) includes the poorly understood Perseus-to-Sagittarius Interarm

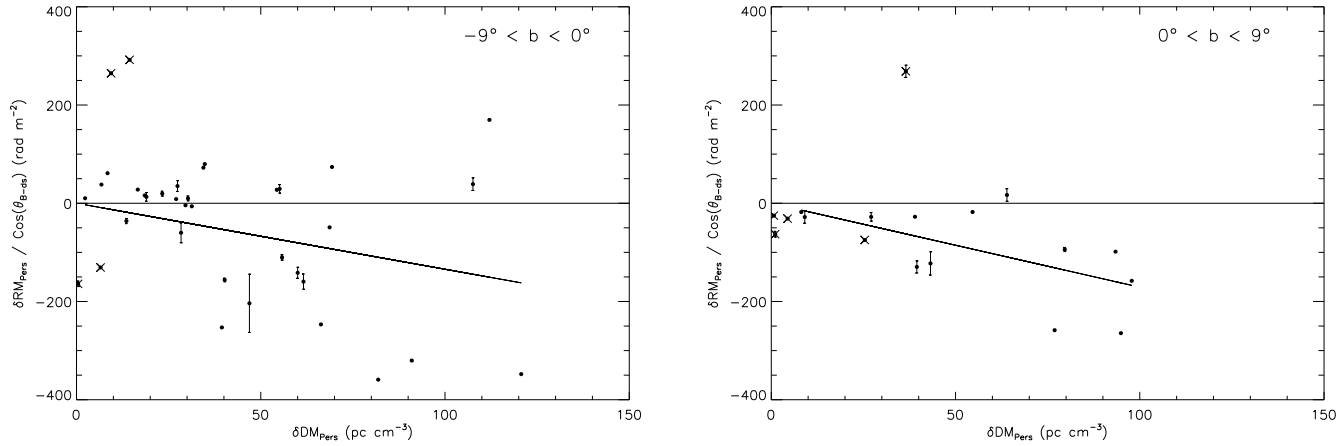

Figure 14. Same as Figure 3, but for pulsars in the Perseus Arm. We truncate the right panel at $\delta\mathrm{RM}_{\mathrm{Pers}} = [-500, 500]$ rad m^{-2}, and hence two outliers at ($\delta\mathrm{RM}_{\mathrm{Pers}}$, $\delta\mathrm{DM}_{\mathrm{Pers}}$) = (735.79 rad m^{-2}, 63.24 pc cm^{-3}) and (-1267.22 rad m^{-2}, 17.41 pc cm^{-3}) are not shown. We also truncate the plot at $\delta\mathrm{DM}_{\mathrm{Pers}} < 150$ pc cm^{-3}, with an outlier at ($\delta\mathrm{RM}_{\mathrm{Pers}}$, $\delta\mathrm{DM}_{\mathrm{Pers}}$) = ($-307.25$ rad m^{-2}, 349.79 pc cm^{-3}) not shown. All outlier information (including these two) is listed in Table 3.

(see Section 4.6), and hence the field reversal could also be due to a CCW magnetic field within the interarm. These authors similarly do not apply any geometrical corrections.

J. L. Han et al. (2018) also use the RMs of EGSs to deduce a switch in the magnetic field direction between the Local Arm and the location of EGSs in the longitude interval of $80° < l < 120°$. They locate this switch to the Perseus Arm, although it cannot be definitively located with EGSs. Using our updated sample of pulsars, we model the same wedge region of $80° < l < 120°$ and do not find any field reversal within the Perseus Arm, so the reversal must lie somewhere beyond it.

4.8. Norma-Outer Arm and Perseus-to-Norma Interarm

J. Rankin et al. (2023) greatly increased the number of pulsars with RMs in the Perseus-to-Norma Interarm and the Norma-Outer Arm (see, e.g., Figure 1). However, even with this increase, there are still an insufficient number of pulsars within these two regions to do proper studies of the magnetic field. With the increasing sensitivity of radio telescopes, though, more pulsars will undoubtedly be found within these regions, and our technique can then be applied to them.

5. Comparison of Our Results with Galactic Magnetic Field Models

Mapping the magnetic field structure within galaxies (both our own and external ones) is important for understanding how galaxies form and evolve. The magnetic structure affects processes such as cosmic-ray propagation, the outflow of gas, and the star formation rate (R. Beck 2016). Additionally, understanding the magnetic field structures of spiral galaxies gives essential insight into the formation of the Milky Way.

5.1. Observations and Theories of Spiral Galaxy Magnetic Fields

Observations of external spiral galaxies have revealed that the magnetic field typically follows the spiral structure, with the magnetic field pitch angle similar to that of the optical spiral arms (R. Beck 2016; J. L. Han 2017; M. Krause 2019) and the magnetic field strengths peaking in the interarm regions (but not the arms; see, e.g., NGC 6946; G. Heald et al. 2009). Note, however, that the LOSs probed in external galaxies typically extend to much larger $|z|$ than do Milky Way pulsar observations, so the extragalactic results are not directly comparable to our Galactic measurements.

The magnetic structure within spiral galaxies is most often understood under mean field dynamo theory. In this theory, magnetic fields are generated and maintained by the differential rotation of plasma within the disk of the galaxy, along with turbulent motion due to supernovae, stellar winds, cosmic rays, etc. (referred to as the α-effect). The differential rotation continuously generates a toroidal field, while the α-effect regenerates the poloidal field, creating a self-sustaining magnetic field configuration (see Chapter 5.5 of P. P. Kronberg 2016, for further details on dynamo theory). While a spiral magnetic field structure is supported by dynamo theory, many of the observed details of extragalactic spiral galaxies' magnetic structure are not. For example, extragalactic observations of a similar pitch angle between the optical and magnetic arms, along with a peak in field strength in the interarm regions, are not well explained by the dynamo model (R. Beck 2016; M. Krause 2019).

Under mean field dynamo theory, different modes are possible for the azimuthal symmetries of the magnetic field within the disk of a spiral galaxy (R. Beck 2016). The most common dynamo mode is one in which the magnetic field in the disk is an axisymmetric spiral (ASS). M31 has such a field (R. Beck 2016). However, a dynamo model could also support a bisymmetric spiral (BSS) magnetic field configuration in which there is a single reversal of the field direction at a given disk radius (see Figure 5.7 in P. P. Kronberg 2016, for further discussion of the difference between an axisymmetric and bisymmetric magnetic field configuration). A bisymmetric magnetic field configuration within a galaxy has yet to be conclusively confirmed, although it is posited that M81 may have such a structure (R. Beck 2016).

5.2. Past Efforts to Model the Galactic Magnetic Field

There have been multiple efforts to use various types of observations to constrain models of the Galactic magnetic field. The most common models advanced include an ASS model, a BSS model, and an ASS + ring model. In the last model, the ASS field is overlaid by a field reversal within a narrow ring at a given Galactic radius. Below, in order to give context to our efforts, we give brief overviews of some of the recent efforts to fit these models to pulsar and/or EGS RMs plus additional

Table 4
Overview of Relevant Galactic Magnetic Field Models

Reference	Input Data[a]	Notable Results[b]
X. H. Sun et al. (2008)	EGS RMs; all-sky intensity and polarization maps	*Disk field*: CW ASS field with a CCW ring between the Carina–Sagittarius Arm and the Crux–Scutum Arm. *Toroidal halo field:* odd z-parity.
H. Men et al. (2008)	Pulsar RMs	*Disk field*: neither ASS, BSS, nor ASS + ring models fit the data.
C. L. Van Eck et al. (2011)	EGS RMs; pulsar RMs	*Disk field*: CW ASS field in inner Galaxy with a single CCW spiral interior to the Local Arm; CW ring in outer Galaxy.
R. Jansson & G. R. Farrar (2012)	WMAP7 Galactic synchrotron emission; EGS RMs	*Disk field*: one azimuthal ring between 3 and 5 kpc; eight spiral arms with multiple field reversals. *Toroidal halo field*: field has z-asymmetry.
J. L. Han et al. (2018)	Pulsar RMs	*Disk field*: field follows the spiral arms with field reversals at the boundaries of some arms and interarms.
J. Xu et al. (2022)	Pulsar RMs	*Disk field*: similar to J. L. Han et al. (2018).
J. M. Dickey et al. (2022)	GMIMS FD spectra of the diffuse Galactic synchrotron emission; EGS RMs	*Disk field*: spiral or azimuthal disk field. *Toroidal halo field:* field has z-asymmetry.
M. Unger & G. R. Farrar (2024)	WMAP and Planck Galactic synchrotron emission; EGS RMs	*Disk*: grand-design spiral with alternating-sign magnetic arms, with magnitude anticorrelated with other spiral tracers; alternatively, Local Spur model fits adequately. *Toroidal halo field*: odd z-parity.
J. Xu & J. L. Han (2024)	EGS RMs; pulsar RMs	*Toroidal halo field*: odd z-parity.

Notes.
[a] Type of data used to perform the Galactic magnetic field analyses.
[b] Brief summary of relevant model results.

types of data in some cases. We also list the relevant details of each model in Table 4.

5.2.1. Axisymmetric and Axisymmetric + Ring Models

We first focus on observations and analyses that appear to be best described by an ASS Galactic magnetic field with or without a ring. X. H. Sun et al. (2008) use the RMs from EGSs, along with all-sky intensity and polarization maps, to study the Galactic magnetic field. They find that the best model comprises a CW, ASS magnetic field atop most arms, with a CCW magnetic ring generally between the Carina–Sagittarius and Crux–Scutum Arms. This result is similar to that of C. L. Van Eck et al. (2011), who, using the RMs of EGSs, find that the inner Galactic magnetic field points largely CW along spiral arms, except for a single CCW spiral field interior to the Local Arm.[17] In the outer Galaxy, the field is consistent with a CW azimuthal field (see Figure 11 of C. L. Van Eck et al. 2011). This model is similar to the model of X. H. Sun et al. (2008), which consists of a CW ASS field with a single CCW ring near the Sagittarius Arm. Interestingly, the major magnetic spiral feature in the C. L. Van Eck et al. (2011) model overlays the generally accepted Carina–Sagittarius Arm location in the first Galactic quadrant, but not in the other three quadrants.

5.2.2. Higher-order Models

We next focus on observations that are not well fit by the simpler models described above. For example, H. Men et al. (2008) use pulsar RMs and find that neither an ASS, BSS, nor ASS + ring model can adequately fit the measurements. Instead, they conclude that a more complex model is needed. J. L. Han et al. (2018) similarly use pulsar RMs and find that the field follows the spiral arms with field reversals at the boundaries of some arms and interarms. J. Xu et al. (2022) find similar results using the same technique as J. L. Han et al. (2018) but with a larger sample of pulsar RMs.

M. Unger & G. R. Farrar (2024) used RMs from EGSs to fit for different grand spiral configurations. Their best-fitting model has six magnetic arms with field magnitudes peaking in the interarms with near-zero field strength at the arm centers. This is consistent with some observations of extragalactic spirals (see Section 5.1), but not with most Galactic models. However, the RMs used by M. Unger & G. R. Farrar (2024) are also fit approximately equally well with a model in which the magnetic field is zero everywhere except the Local Arm, where it is strong ($\sim 4\,\mu$G) and CCW. This demonstrates a major difficulty in using solely EGS RMs to model the Galactic magnetic field, as they do not explicitly encode Galactic distance information in the same way as pulsars.

5.2.3. Magnetic Field Disparities above and below the Galactic Plane

X. H. Sun et al. (2008), R. Jansson & G. R. Farrar (2012), J. M. Dickey et al. (2022), M. Unger & G. R. Farrar (2024), and J. Xu & J. L. Han (2024) have all found evidence for a toroidal (i.e., longitudinal) halo field that extends to high $|z|$ and has different properties above and below the Galactic plane. In particular, all of the above authors find that the toroidal halo field has opposite signs above and below the Galactic equator.

[17] For our purposes, the "inner Galaxy" refers to that portion lying within the solar circle.

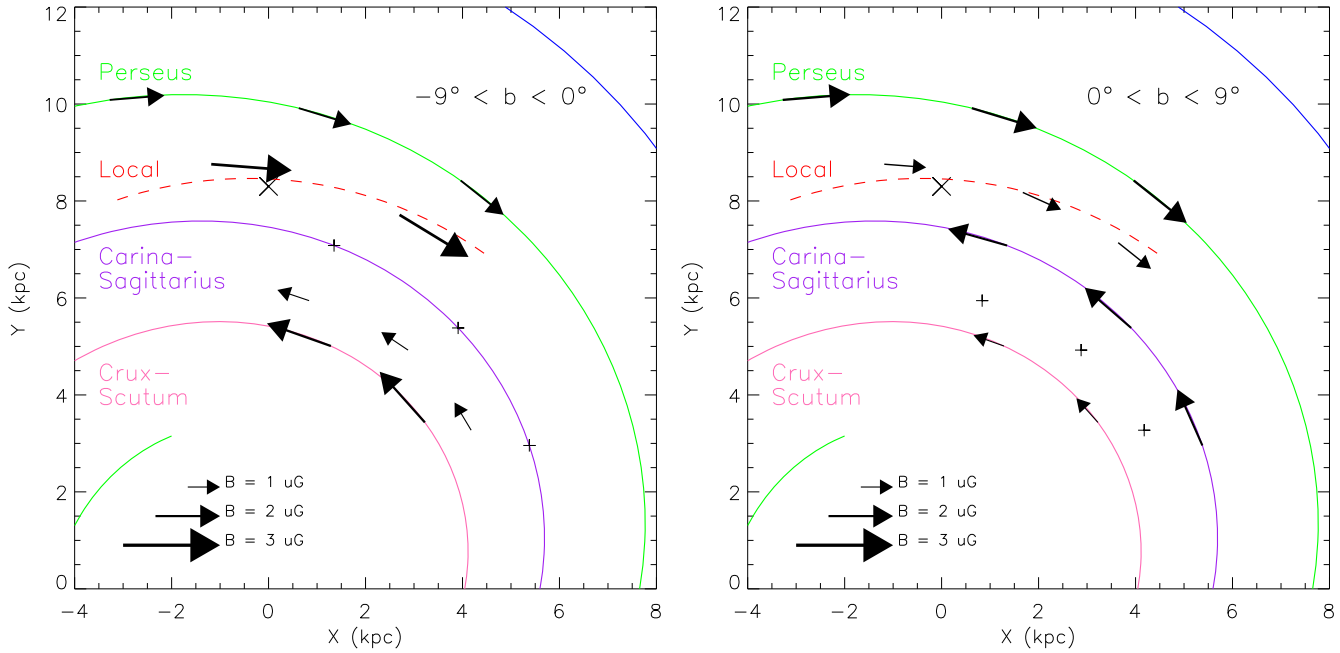

Figure 15. Left: the derived magnitudes and directions of the large-scale, planar magnetic field for negative Galactic latitudes. The magnetic field vectors are displayed atop the centers of the associated arms, except for the Sagittarius-to-Scutum Interarm field, which is shown between the Sagittarius and Scutum Arms. Arrow sizes are directly proportional to the magnitude of the magnetic field, while the arrow directions indicate whether the derived field is CW or CCW. Zones with derived magnetic field strengths less than their 1σ uncertainty are shown with crosses. See Table 1 for exact magnitudes and their uncertainties. Right: same as the left panel, but for positive Galactic latitudes.

At low $|z|$, the Sagittarius Arm's longitudinal field also exhibits an asymmetry between positive and negative latitudes, as was previously noted (see A. Ordog et al. 2017; Y. K. Ma et al. 2020; our Section 4.3).

5.3. Our Work in Context

We now discuss our results in the context of the above Galactic magnetic field models. To summarize our work, we show our best-fit low-latitude magnetic field directions and magnitudes in our zones of study in Figure 15, with negative (positive) Galactic latitudes plotted separately in the left (right) panel.

5.3.1. Measured Field Strengths above and below the Galactic Midplane

Our measured differences in the disk field strength (though not its direction) at positive and negative Galactic latitudes in several zones could be a result of combining the disk's stronger z-symmetric longitudinal field with the halo's weaker z-asymmetric or odd z-parity toroidal fields if these toroidal fields extend down into the Galactic disk (see Section 5.2.3 and Table 4). If these toroidal fields are indeed significant in the Galactic disk, then we would expect our measured B-fields above the plane to tend more positive (i.e., CCW) than those below the plane. The models, however, suggest that the toroidal halo fields decline sharply toward the plane. Additionally, we do not see consistent evidence for the asymmetry in all regions.

5.3.2. Field Reversal in the Disk within the Solar Circle

Both above and below the Galactic plane, we find evidence for only a single field reversal throughout all the Galactic regions we studied, lying at or near the Sagittarius Arm−Local Arm boundary. In Figure 16, we show our derived Sagittarius Arm B-fields along specific pulsar LOSs, with negative Galactic latitude pulsars shown in the left panel and positive Galactic latitude pulsars shown in the right panel. At positive Galactic latitudes, the strength and direction (CCW) of the B-field in the Sagittarius Arm are relatively constant, indicating that the field reversal occurs between the Local (CW) and Sagittarius (CCW) Arms. However, at negative Galactic latitudes, the CW-to-CCW field reversal occurs inside of the Sagittarius Arm itself. Therefore, the reversal apparently conforms to spiral structure in the plane but tilts toward (away from) the Galactic center south (north) of the Galactic plane.

Studying the total RMs of EGSs and pulsars, A. Ordog et al. (2017) also found evidence of a dependence on Galactic latitude and longitude for the field reversal from a CW to a CCW field near the Sagittarius Arm. They note that the signs of the total RMs in the region bounded by $56° \lesssim l \lesssim 67°$ and $-3° < b < 5°$[18] are mostly separated on the sky by a diagonally tilted line (hereafter referred to as the Ordog et al. line) extending from $(l,\ b) = (56°,\ -2°)$ to $(l,\ b) = (67°,\ 4°)$. However, their EGS and Galactic synchrotron RM measurements do not yield the distance to the sampled objects, so (as they note) their "line" might be merely the projection onto the plane of the sky of a more complicated topology such as a tilted planar object. It is also important to note that the "line" is not a physical object but merely an imaginary boundary separating RMs of different signs.

In contrast to A. Ordog et al. (2017), our analysis techniques separate RMs and B-fields by arm, thereby yielding information on distance, a spatial dimension that has been mostly absent in previous analyses. In Figure 17, we show our derived Local and Sagittarius Arm B-fields in approximately the same longitude and latitude region as that studied by A. Ordog et al.

[18] This corresponds to the approximate longitude range of the tangent to the Sagittarius Arm.

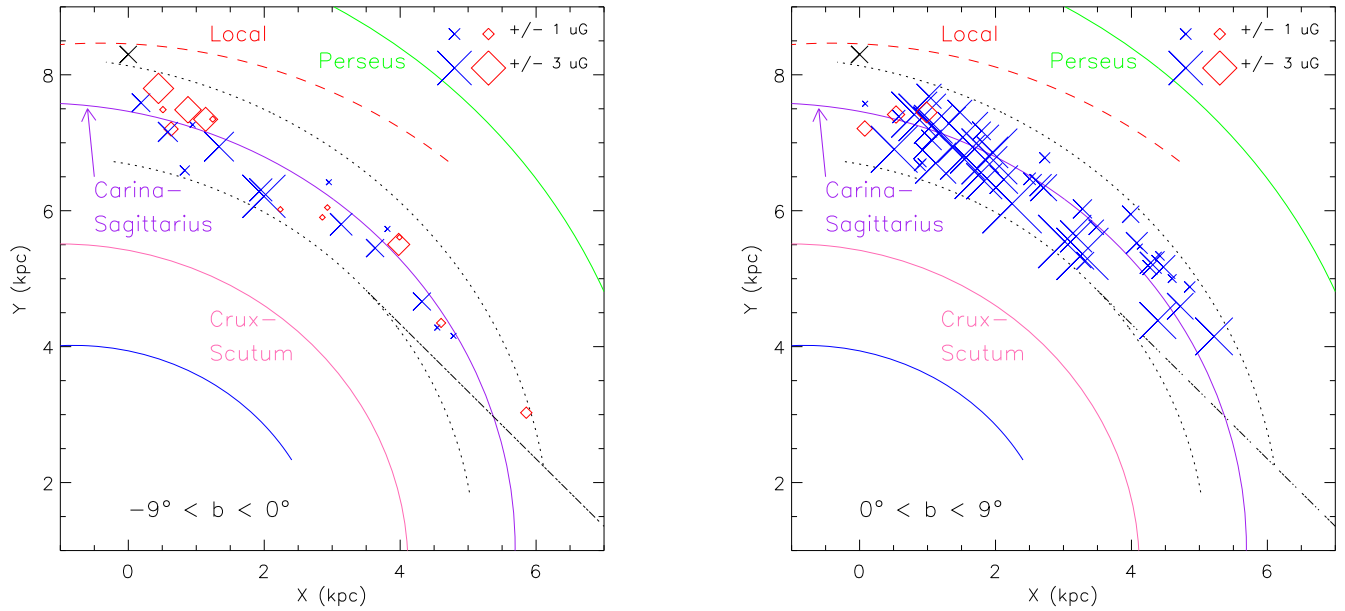

Figure 16. Left: longitudinal magnetic fields at negative Galactic latitudes in the Sagittarius Arm, derived from pulsars at the displayed locations. The Sagittarius Arm center is delineated and labeled in purple, with its inner and outer boundaries shown by flanking black dotted lines. A CCW magnetic field ("positive" by our convention) is shown as a blue cross, while a CW magnetic field ("negative" by our convention) is indicated with a red diamond. The solar system is marked by the black cross at $(x, y) = (0.0, 8.3)$ kpc. Outliers (listed in Table 3) are not shown. Right: same as the left panel, except at positive Galactic latitudes.

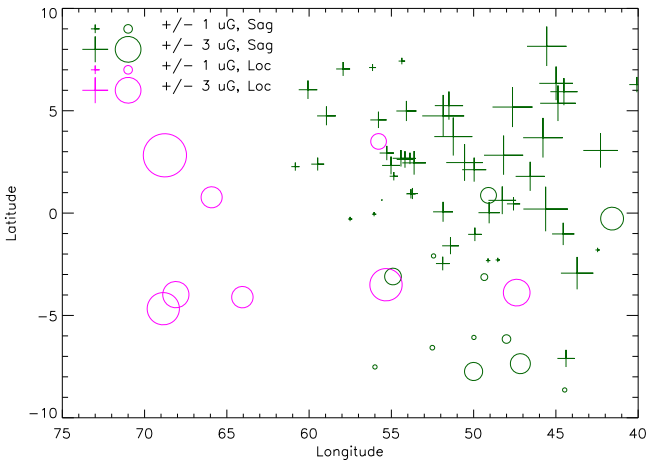

Figure 17. Magnetic field strengths measured in this work along the Local Arm (magenta) and the Sagittarius Arm (green) in the approximate longitude and latitude regions studied by A. Ordog et al. (2017). Magnetic field direction along an arm is indicated with a cross (positive, CCW) or a circle (negative, CW), with its magnitude shown via the symbol's size. For pulsars for which $|B| < 0.5$ μG, we set the symbol size to be equivalent to that of $|B| = 0.5$ μG. Similarly, for any pulsars for which $|B| > 20$ μG, we set the symbol size to be equivalent to that of $|B| = 20$ μG. Outliers (listed in Table 3) are not shown.

(2017).[19] Consistent with their results, we find that the CW "negative" fields are predominantly found toward higher l and lower b (i.e., below the Ordog et al. line) while the CCW "positive" fields are primarily located toward lower l and higher b (i.e., above the Ordog et al. line). Given our ability to distinguish between the Local and Sagittarius Arms, we note that the majority of the trends discussed above are naturally accounted for by our and others' results of a CW field in the Local Arm switching to a CCW field in the Sagittarius Arm.

[19] We extend their longitude range to include a larger portion of the Sagittarius Arm.

It is interesting to note that the few Sagittarius Arm LOSs with CW "negative" B-fields primarily lie below the Ordog et al. line, which is unlike the positive Sagittarius B-field LOSs located above the line. Additionally, as discussed above, we find a latitude-dependent location of the field reversal near the Local and Sagittarius Arms. If the Ordog et al. line were in a quasi-planar object that follows the shape of the Sagittarius Arm−Local Arm boundary and is tilted toward the Galactic center at negative Galactic latitudes, it could explain both our above results and those of A. Ordog et al. (2017), as it would predict that the reversal at negative Galactic latitudes would occur at smaller Galactic radii than the reversal at positive latitudes. However, given the complexity of this region and the possible underlying progenitors of the magnetic field, we leave further investigation of this to future work.

5.3.3. Comparison to External Spiral Galaxy Magnetic Fields

In both the best-fit Galactic model by M. Unger & G. R. Farrar (2024) and many observations of external spiral galaxies (G. Heald et al. 2009; R. Beck 2016), the magnetic field strength peaks between arms, with negligible field strengths within them. Our negligible field strength measurements in the negative Galactic latitude Sagittarius Arm thus agree both with the M. Unger & G. R. Farrar (2024) model and with extragalactic spiral galaxies' magnetic field observations. However, no other zone that we analyzed is consistent with this picture. Notably, the magnetic field within the one distinctive interarm region that we studied, the Sagittarius-to-Scutum Interarm region, is consistent with zero at negative Galactic latitudes and relatively weak at positive Galactic latitudes.

5.3.4. Bisymmetric Model

Both above and below the plane, our RM values support a bisymmetric model that includes at least one magnetic field reversal. It is possible that there are more magnetic field reversals interior to the Scutum Arm or beyond the Perseus

Arm, as these zones are not modeled in this work. A bisymmetric model is in general agreement with recent efforts to study the Galactic magnetic field in the disk (e.g., J. L. Han et al. 2018; J. Xu et al. 2022; M. Unger & G. R. Farrar 2024). However, the field reversals and field directions derived in this work disagree with many of those previously published. We attribute this to different analysis procedures, particularly our improved technique that accounts for intervening arms' RM contributions and the dot-product nature of Faraday rotation.

6. Summary

In this work, we develop a new technique for using the observed total RMs of an ensemble of pulsars to study the large-scale Galactic magnetic field under the assumption that the field follows the spiral arms. We split the observed total RM and DM of a given pulsar into segments corresponding to different spiral arms or interarm zones along a given LOS. Starting with the Local Arm, we solve for its magnetic field strength while accounting for the dot-product nature of the RM-defining integral. We then recursively move to zones farther from Earth, using our calculation of the inner zones' magnetic field strengths to determine and subtract their δRM contributions to the total RM, leaving only the outermost zone's contribution. In this fashion, we are able to assemble an arm-by-arm picture of the Galactic magnetic field within several kiloparsecs of Earth.

We apply our new technique to 313 low Galactic latitude pulsar RMs published in J. Rankin et al. (2023), along with other pulsar RMs within and adjoining the same regions (approximately the first Galactic quadrant and a section of the third Galactic quadrant). Our technique adds approximate distance information to otherwise two-dimensional RM analyses. Its prime application is in separating spiral arms along an LOS for individual study, but we also show its utility in providing likely explanations for puzzling features in the total RM sky.

We determine the magnetic field strength along the Local Arm, the Sagittarius Arm, the Sagittarius-to-Scutum Interarm, and the Perseus Arm. We find disparities $>1\sigma$ for the magnetic field strength (though not its direction) above and below the plane in most zones studied, with the greatest disparity in the Sagittarius Arm.

We find only one major arm-to-arm (or arm-to-interarm) field reversal throughout all the zones we investigate, although its Galactocentric location varies slightly between positive and negative Galactic latitudes. At positive b the field reversal occurs between the Local (CW) and Sagittarius (CCW) Arms, while at negative b the reversal appears to occur within the Sagittarius Arm itself.

Our results favor a bisymmetric model for the large-scale Galactic magnetic field with at least one field reversal inside the solar circle. It is possible that there are more reversals beyond our current region of study, either inside the Scutum Arm or outside the Perseus Arm, but we leave analysis of these zones to future work. A bisymmetric model is in agreement with most recently published works on the Galactic magnetic field (J. L. Han et al. 2018; J. Xu et al. 2022; M. Unger & G. R. Farrar 2024). However, unlike observations of external spiral galaxies and certain Galactic models, we find that the magnetic field is usually strongest within arms rather than between then.

We expect that the geometrically corrected "arm-by-arm" technique presented here will continue to be useful as additional pulsars' RMs and DMs are measured. Future work could then extend this analysis to farther regions of the Galaxy.

Acknowledgments

The authors gratefully acknowledge financial support from the US National Science Foundation, under grants AST-1312843 (A.P.C. and J.W.) and 18-14397 (J.M.R.). The Arecibo Observatory was operated by the University of Central Florida under a cooperative agreement with the US National Science Foundation and in alliance with Yang Enterprises and the Ana G. Méndez-Universidad Metropolitana. A.P.C is a Vanier Canada Graduate Scholar.

Facility: Arecibo.

Appendix
Pulsars Whose LOSs Intersect the Gum Nebula

Table A1 lists those pulsars in our sample whose LOSs intersect the Gum Nebula. As noted in Section 4.1, this nebula has a complicated and poorly known magnetic structure, so we exclude these pulsars from our fits.

Table A1
Pulsars in Our Sample Lying within or beyond the Gum Nebula

PSR	l (deg)	b (deg)	DM (pc cm^{-3})	Distance (kpc)
J0737−3039A/B	245.2	−4.5	48.9	1.1
B0736−40	254.2	−9.2	160.9	1.6
B0740−28	243.8	−2.4	73.7	2.0
J0749−4247	257.1	−8.3	104.6	0.6
B0808−47	263.3	−8.0	228.3	6.5
J0818−3232	251.4	1.9	131.8	0.5
J0820−3826	256.5	−1.0	195.6	4.1
J0820−3921	257.3	−1.6	179.4	3.6
B0818−41	258.7	−2.7	113.4	0.6
J0821−4221	259.8	−3.1	270.6	5.8
B0826−34	254.0	2.6	52.2	0.4
J0831−4406	262.3	−2.7	254.0	5.9
J0834−4159	260.9	−1.0	240.5	5.5
J0835−3707	257.1	2.0	112.3	0.6
B0835−41	260.9	−0.3	147.3	1.5
J0838−2621	248.8	9.0	116.9	4.1
B0839−53	270.8	−7.1	156.5	0.6
B0840−48	267.2	−4.1	196.8	3.1
J0843−5022	268.5	−4.9	178.5	1.6
B0844−35	257.2	4.7	94.2	0.5
B0853−33	256.8	7.5	86.6	0.5
J0855−4644	267.0	−1.0	236.4	5.6
J0855−4658	267.1	−1.2	472.7	13.7
J0857−4424	265.5	0.8	184.4	2.8
J0900−3144	256.2	9.5	75.7	0.9
J0901−4624	267.4	−0.0	199.3	3.0
B0903−42	265.1	2.9	145.8	0.7
J0905−4536	267.2	1.0	179.7	2.0
J0905−5127	271.6	−2.9	196.4	1.3
J0905−6019	278.2	−8.8	91.4	0.4
B0905−51	272.2	−3.0	103.7	0.3
B0906−49	270.3	−1.0	180.4	1.0
J0912−3851	263.2	6.6	71.5	0.3
J0922−4949	272.2	0.2	237.1	2.7
B0922−52	274.7	−1.9	152.9	0.5
B0932−52	275.7	−0.7	100.0	0.3
J0940−5428	277.5	−1.3	134.6	0.4
J0941−5244	276.4	0.1	157.9	0.4
B0941−56	279.3	−3.0	159.7	0.4
J0945−4833	274.2	3.7	98.1	0.4
J0954−5430	279.0	−0.1	201.6	0.4
B0953−52	278.3	1.2	156.9	0.4
J0957−5432	279.4	0.2	226.1	0.4
B0957−47	275.7	5.4	92.7	0.4
J1001−5559	280.7	−0.6	159.3	0.4
B1001−47	276.0	6.1	98.5	0.4
B1011−58	283.7	−2.1	383.9	3.2
J1013−5934	284.1	−2.6	379.8	3.1
J1015−5719	283.1	−0.6	278.1	2.7
J1016−5819	283.7	−1.4	252.2	2.6
J1016−5857	284.1	−1.9	394.5	3.2
B1015−56	282.7	0.3	438.7	3.5
J1019−5749	283.8	−0.7	1040.0	10.9
J1020−6026	285.3	−2.8	441.5	3.3
J1036−4926	281.5	7.7	136.5	2.3

ORCID iDs

Alice P. Curtin https://orcid.org/0000-0002-8376-1563
Joel M. Weisberg https://orcid.org/0000-0001-9096-6543
Joanna M. Rankin https://orcid.org/0000-0002-8923-6065

References

Beck, R. 2016, A&ARvAdSpR, 24, 4
Dickey, J. M., West, J., Thomson, A. J. M., et al. 2022, ApJ, 940, 75
Efron, B., & Tibshirani, R. 1991, Sci, 253, 390
Griv, E., Jiang, I.-G., & Hou, L.-G. 2017, ApJ, 844, 118
Han, J. L. 2017, ARA&A, 55, 111
Han, J. L., Manchester, R. N., van Straten, W., & Demorest, P. 2018, ApJS, 234, 11
Heald, G., Braun, R., & Edmonds, R. 2009, A&A, 503, 409
HI4PI Collaboration, Bekhti, N., & Flöer, L. 2016, A&A, 594, A116
Hou, L. G., & Han, J. L. 2014, A&A, 569, A125
Jansson, R., & Farrar, G. R. 2012, ApJ, 757, 14
Johnston, S., Sobey, C., Dai, S., et al. 2021, MNRAS, 502, 1253
Kirichenko, A., Danilenko, A., Shternin, P., et al. 2015, ApJ, 802, 17
Krause, M. 2019, Galax, 7, 54
Kronberg, P. P. 2016, Magnetic Field Configurations in Large Galaxies, in Cosmic Magnetic Fields (Cambridge: Cambridge Univ. Press), 72
Kutukcu, P., Ankay, A., Yazgan, E., & Bozkurt, K. 2022, MNRAS, 511, 4669
Lorimer, D. R., & Kramer, M. 2012, Handbook of Pulsar Astronomy (Cambridge: Cambridge Univ. Press)
Ma, Y. K., Mao, S. A., Ordog, A., & Brown, J. C. 2020, MNRAS, 497, 3097
Manchester, R. N. 1972, ApJ, 172, 43
Manchester, R. N., Hobbs, G. B., Teoh, A., & Hobbs, M. 2005, AJ, 129, 1993
Men, H., Ferrière, K., & Han, J. L. 2008, A&A, 486, 819
Mitra, D., Wielebinski, R., Kramer, M., et al. 2003, A&A, 398, 993
Ocker, S. K., Anderson, L. D., Lazio, T. J. W., et al. 2024, ApJ, 974, 10
Ohno, H., & Shibata, S. 1993, MNRAS, 262, 953
Ordog, A., Brown, J. C., Kothes, R., et al. 2017, A&A, 603, A15
Purcell, C. R., Gaensler, B. M., Sun, X. H., et al. 2015, ApJ, 804, 22
Rankin, J., Venkataraman, A., Weisberg, J. M., & Curtin, A. P. 2023, MNRAS, 524, 5042
Reid, M. J., Dame, T. M., Menten, K. M., & Brunthaler, A. 2016, ApJ, 823, 77
Reid, M. J., Menten, K. M., Brunthaler, A., et al. 2019, ApJ, 885, 131
Shanahan, R., Lemmer, S. J., Stil, J. M., et al. 2019, ApJL, 887, L7, S19
Sun, X. H., Reich, W., Waelkens, A., et al. 2008, A&A, 477, 573
Unger, M., & Farrar, G. R. 2024, ApJ, 970, 95
Van Eck, C. L., Brown, J. C., Stil, J. M., et al. 2011, ApJ, 728, 97
Weisberg, J. M., Cordes, J. M., Kuan, B., et al. 2004, ApJS, 150, 317
Xu, J., Han, J., Wang, P., & Yan, Y. 2022, SCPMA, 65, 129704
Xu, J., & Han, J. L. 2019, MNRAS, 486, 4275
Xu, J., & Han, J. L. 2024, ApJ, 966, 240
Xu, Y., Bian, S. B., Reid, M. J., et al. 2018, A&A, 616, L15
Xu, Y., Li, J. J., Reid, M. J., et al. 2013, ApJ, 769, 15
Yao, J. M., Manchester, R. N., & Wang, N. 2017, ApJ, 835, 29